ᵁS

FACULTY OF SCIENCE AND TECHNOLOGY

MASTER THESIS

Study programme / specialisation:

Marine and Offshore Technology

The spring semester, 2022

Open / ~~Confidential~~

Author: Trygve Pollen

..........*Trygve Pollen*..............
(signature author)

Course coordinator: Prof. Yihan Xing

Supervisor(s): Prof. Muk Chen Ong, Dr. Guang Yin

Thesis title: Numerical Study of Oxygen Transport in Aquaculture Tanks With Different Geometries

Credits (ECTS): 30

Keywords:

CFD, Aquaculture, OpenFOAM, Dissolved oxygen, VOF, Diffusion, Water tank, Convection

Pages: ....71 ......

+ appendix: ....0......

Stavanger, ...15/06/2022.....
date/year

Abstract

The transport of dissolved oxygen concentration in water for aquaculture is a core parameter affecting the quality of yielded fish. An emerging shift from offshore to land-based aquaculture presents advantages to marine ecosystem sustainability and the maintenance fish health. One primary engineering challenge of migrating aquaculture production to land-based facilities is developing sustainable aquatic conditions for fish.

The objective of the present study is to use OpenFOAM CFD to simulate oxygen transport in different water tank geometries based on the study performed by Yin et al. (2021) as a starting point. A $5.0m$ diameter circular tank geometry and three rounded square tank geometries with different corner diameters ($2.0m$, $1.5m$, $1.0m$) are used in the study. The tanks are compared to see how the shape of the tank influences the oxygen transport in the water. Numerical studies are performed using a transient multi-phase CFD solver to obtain results for the four different geometries. The tanks are filled with water until a steady state is reached for the oxygen concentration. Point measurements are then extracted from the flow domain for comparing the spatial distribution of the diffused oxygen. The results of the study show that the circular water tank geometry most suited at transporting diffused oxygen in the water tank with steady radial water flow. The square tank geometries showed an overall reduction in flow velocity in the flow domain which is further diminished with smaller corner radius. Different with the circular geometry, the lack of rotational symmetry causes the momentum change of the water to create skewed flow in the square tanks.

The circular geometry is considered in a mesh convergence study to determine an optimal mesh resolution for the simulation. A validation study of oxygen transport in circular tank geometry is conducted using experimental data for comparison. The comparison showed the numerical results to have a maximum difference of 9% for probes close to the inlet.

Moreover, the results are valuable as a starting point for design of tank geometries and their ability to circulate oxygen in aquaculture tanks. The numerical results give an insight to the physical quantities in the water flow which is important to consider in the selection of water tank designs for land-based aquaculture.

Acknowledgments

Contents

List of Figures

List of Tables

1 Introduction

1.1 Background and motivation

Aquaculture production is an important asset of the offshore industry and food production in Norway. The majority of the aquaculture facilities in Norway are located along the western shores bordering the North Sea and make up for most of the production volume. A typical offshore aquaculture facility uses floating pens to cultivate fish. These pens are partially submerged in water and allow fish to move freely around within a closed body of water. The installations' design allow for sea water circulation using the water current. This allows the facility to function without auxiliary aeration systems, although these can be added to increase sustainable capacity of livestock within a cage.

The alternative to marine aquaculture is land-based aquaculture. This farming method is gaining popularity among large players in the industry. Existing land-based aquaculture producers are increasing planned production volume and new companies want to join the market, according to Moe et al. (2020). Existing land-based aquaculture facilities use water tanks to grow livestock in their spawning phase before being placed in fish farms (Misund, 2011).

Discussions regarding the advantages and disadvantages for sea-based or land-based aquaculture production has been a popular topic in recent years. Impact on environment, ecosystem and marine conditions of each farming method raise the question of which approach is better. A transition to land-based facilities could become a future trend for sustainability according to Venvik (2020).

An engineering challenge behind land-based aquaculture is being able to create a sustainable and thriving aquatic environment to cultivate healthy fish. The success of land-based aquaculture is dependent to the ability to provide dissolved oxygen to the fish within the aquaculture tanks. The convection of diffused oxygen in a water tank is dependent on the flow of the water. The geometry of the tank affects the flow direction and velocity of the water. The distribution of oxygen is thus dependent on the tank geometry. The aim of the study is to simulate and compare the effect on spatial distribution of diffused oxygen in land-based aquaculture with different geometries of water tanks.

1.2 Thesis scope and objectives

The primary objective of the present study is to predict oxygen concentration distributions in the water of different shapes of onshore aquaculture tanks using CFD (computational fluid dynamics). It requires a computational model setup with defined initial conditions and boundary conditions to perform the simulations. The data outputs from the simulations are post-processed to analyze the oxygen distribution and the flow velocity distribution under different conditions. Four different water tank designs will be chosen for simulation with a varying shape from circular to a square-shaped design. The study will be based on the work conducted by Yin et al. (2021). The study is centered around the use of OpenFOAM, which is a computational fluid dynamics (CFD) software to perform the simulation of oxygen transport and flow inside the tanks.

1.3 Organization of the present study

The thesis is chronologically structured to explain the applied theory and work process from introduction to conclusion. Firstly the objective of the thesis is defined and scope outlined. Supporting theory of fluid mechanics relevant for the CFD numerical method is presented before the computational setup is introduced. A convergence study is performed to determine the accuracy of the computational model. A validation study is performed to evaluate the numerical results' prediction with experimental results. The convergence and validation studies are performed using the obtained results from the circular water tank geometry. The results from all the investigated geometries are presented and discussed in the results section. Data comparison across all the cases is conducted after the individual results are discussed. Conclusions regarding the geometries' effect on oxygen transport are drawn in the end of the thesis.

2 Theory

2.1 Flow model

This chapter focuses on core equations of fluid motion and mathematical theory related to CFD simulation. The equations presented are useful for explaining the steps for how the solver obtains results. Most of the equations are primarily used for explaining the foundational principles of the computational model. The two main components of the theory applied in the CFD portion are related to the fluid motion and the diffusion of matter, such as the dissolved oxygen considered in the present study.

2.1.1 Governing equations of the fluid

The continuity equation is based on a conservation law in fluid mechanics. It establishes mass conservation for fluid flow in a control volume. A control volume is an arbitrary space with fluid. The continuity equation affects the control volume by ensuring that the mass of the fluid coming into the volume is equal to the mass of the flow leaving the control volume.

A one-dimensional example of applying the law is steady flow through a pipe. A pipe has an inlet and outlet which fluid is transported continuously. The mass of fluid entering the inlet will be equal to the mass of fluid exiting the outlet for a steady flow. There can be no fluid added or removed in the control volume that does not pass through either the inlet or outlet. The conservation law is applicable to open cell volumes, where the mass of fluid entering either face of a cell is equal to the mass leaving it from any other face. For an incompressible flow, the density ρ is constant to the system. In turn the fluid velocity $\vec{U}$ and direction defines the law.

$$
\left.\begin{array}{r}
\dfrac{D\rho}{Dt} + \rho(\nabla \cdot \vec{U}) = 0 \\[2mm]
\dfrac{D\rho}{Dt} = 0
\end{array}\right\} \Rightarrow \nabla \cdot \vec{U} = 0
\tag{1}
$$

where each remaining variable is defined as:

$$
\vec{U} = (u, v, w)
\tag{2}
$$

$$
\vec{\nabla} = \left(\frac{\partial}{\partial x}\vec{i} + \frac{\partial}{\partial y}\vec{j} + \frac{\partial}{\partial z}\vec{k}\right)
\tag{3}
$$

The Navier-Stokes equations are based on Newton's second law of motion. Navier-Stokes equation is similar except the mass term is replaced with density, or mass per unit volume. This makes the equation applicable to any size of control volume. The momentum conservation equations are given as:

$$
\rho\frac{D\vec{u}}{Dt} = -\vec{\nabla}P + \rho\vec{g} + \mu\nabla^2\vec{U}
\tag{4}
$$

where

$$\frac{D\vec{U}}{Dt} = \frac{\partial \vec{U}}{\partial t} + \vec{U} \cdot \nabla \vec{U} \tag{5}$$

∇P is the pressure force acting on a finite volume and $\mu \nabla^2 \vec{U}$ is the viscous force acting on a finite volume. ρg is the gravitational force acting on a finite volume as an external force term.

2.1.2   Reynolds Average Navier-Stokes equations (RANS)

Turbulence is a characteristic fluid motion for which flow velocity and direction can fluctuate over time such that the fluid lacks a regular motion pattern. The RANS equation is based on the Reynolds decomposition where a time-dependent flow quantity u can be decomposed into a time-averaged part $\overline{U}$ and a time-independent fluctuation part u'. Equation 6 shows the velocity at a point in time where it is equal to a steady average with a fluctuation over time. The general decomposed equation is written as:

$$u(x,y,z,t) = \overline{U}(x,y,z) + u'(x,y,z,t) \tag{6}$$

where u on the left-hand side is the instantaneous velocity and $\overline{U}$ is calculated using an equation for averaging over a continuous domain (George, 2013):

$$\overline{U}(x,y,z) = \lim_{T \to \infty} \frac{1}{T} \int_{T_1}^{T_2} u(x,y,z,t) dt \tag{7}$$

It is also possible to use the equations for any scalar that is affected by the velocity fluctuation, including the oxygen concentration.

Equation 7 for the present study is only valid for a stationary time-series where the mean quantity is independent of time. Once equilibrium flow is reached in the water tank at T_1, the velocity flow field should have flow quantities that vary with time due to turbulence in the flow, but still have a mean velocity component. The conditions for a time-series average require a non-moving average over time with little dispersion in the oscillation frequency. For a discrete simulation, the average can be written as:

$$\overline{U}(x,y,z) = \lim_{\Delta t \to 0} \frac{1}{T} \sum_{t=T_1}^{T_2} u(x,y,z,t) \Delta t \tag{8}$$

Δt is the write interval used for the simulation. The write interval defines the interval between time steps of the simulation when the flow fields are saved. It is possible to extract data with higher resolution over time, however it requires a reduction in the write interval. An extended time period between sampling can lead to aliasing occurring in the data which does not reflect the real results.
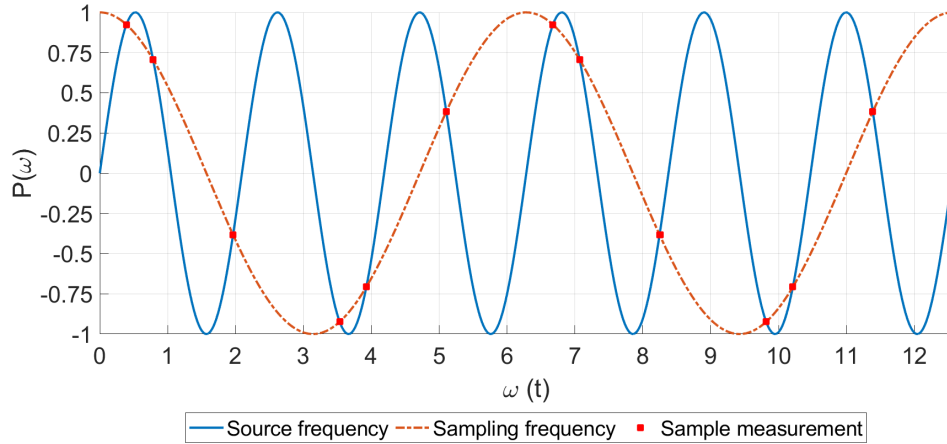
Figure 2.1: Example of aliasing in oscillating data with low sampling rate.

Figure 2.1 shows how sampling rate affects the time-dependent data. It is evident the sampled data does not reflect the true fluctuation frequency. For further detailed study into the turbulence of the water flow, this effect should be taken into consideration.

2.1.3   Boundary conditions

A boundary condition in the field of CFD is a constraint for the simulation environment that affects fluid. A wall surface has conditions that impact the fluid. The no-slip condition means the fluid flow at the surface has zero velocity due to viscous stress denoted as τ_u defined in equation 9. The friction is related to the fluid viscosity μ, which in turn affects the velocity gradient of the fluid as a function of distance from the wall.

$$\tau_u = \mu \frac{du}{dy} \tag{9}$$

The viscosity ν can be converted to kinematic viscosity calculated by;

$$\nu = \frac{\mu}{\rho} \tag{10}$$

The shear stress in the fluid is dependent on the velocity gradient of the fluid. An increased difference in velocity across a small distance, (or thin layer) therefore means there is higher distortion in the fluid. Coupled with the viscosity, the shear increases with viscous fluids. The equation is relevant because the flow velocity in the tank at the inlet region will decelerate due to the fluid shear stress by the wall surfaces, which in turn affects the flow in the rest of the tank volume. The kinematic viscosity of the water is set as $\nu = 1.0 \times 10^{-6} m^2/s$ for the water in the present study.

2.1.4   Courant number

The Courant–Friedrichs–Lewy condition is a useful criterion to ensure the stability of the simulation between time steps. The Courant number C should be lower than 1 for the simulation to be stable.

$$C = \frac{U\Delta t}{\Delta x} \tag{11}$$

The equation is directly used for CFD simulations where a fluids behavior in a transient state is important for interaction between cells. The Courant number is a ratio between the distance covered by a fluid particle and the size of a mesh element Δx within the time step as $U\Delta t$. If the ratio exceeds 1, it means a particle has skipped beyond one cell entirely across the time step. The implication of skipping across cells is the particle motion is a foregone step. The simulation would not account for interactions with another particle entering the skipped cell, thus changing the flow direction. The simulation would then not be as realistic compared to real world model.

2.1.5 Oxygen transport equations (Schmidt number and Henry's law)

The transport equation of the dissolved oxygen are a core of the numerical study in the present study. The transport equations for the oxygen both in the water and in the air are given as:

$$\frac{\partial O_2}{\partial t} + \nabla \cdot (uO_2) = \nabla(D_L \nabla O_2) \tag{12}$$

$$\frac{\partial O_2}{\partial t} + \nabla \cdot (uO_2) = \nabla(D_G \nabla O_2) \tag{13}$$

The volume of fluid (VOF) method is used for the two-phase flow simulation of water and air. The method is used to capture the free surface of the water in a finite volume. The transition layer where water and air makes contact is called the *interface*, which is shown in figure 2.2. Any quantity within a cell is determined by the fraction of fluid. The fraction of fluid α is defined in the conditional equation 14.

$$\alpha = \begin{cases} 0 & \text{for air} \\ 1 & \text{for water} \\ (0,1) & \text{for water \& air interface} \end{cases} \tag{14}$$
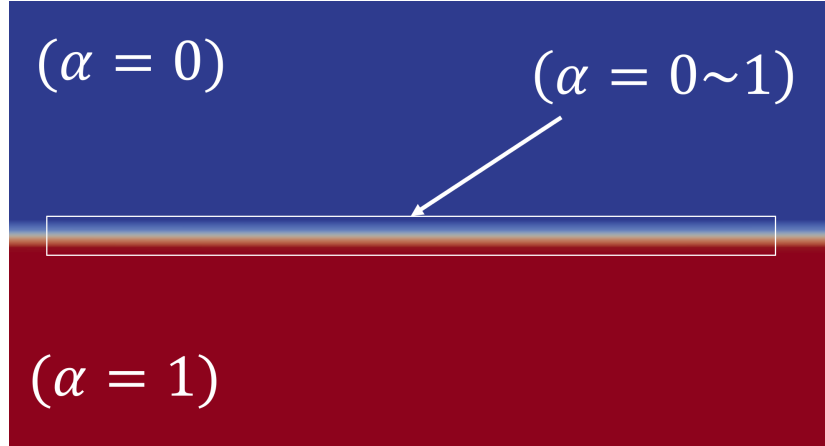
Figure 2.2: Air-water interface visualized in vertical cross section of water surface.

The fluid properties within a cell is based on the VOF method using the fraction of water and air. Linear interpolation can be applied for fluid properties for each medium. Variables such as dynamic viscosity, velocity and density can be calculated using equation 15. χ represents a resultant property for a particular cell based on respective properties for water and air:

$$\chi = \alpha\chi_{water} + (1 - \alpha)\chi_{air} \tag{15}$$

The condition for α as a scalar field can be written as a transport equation which also defines the condition of the scalar field for VOF. The transport equation has two terms, which is the time variation and convection term. The convection term is related to the fluid velocity and the diffusion term is related to the diffusivity and spatial gradient $\nabla\alpha$:

$$\frac{\partial\alpha}{\partial t} + \frac{\partial(\alpha u_j)}{\partial x_j} = 0 \tag{16}$$

The diffusivity constant of a cell as calculated in Yin et al. (2021) is shown in equation 17. The diffusivity property of air and water are based on harmonic averages. The physical diffusion based on VOF can then be obtained.

$$D = \frac{D_G D_L}{(1 - \alpha)D_L + \alpha D_G} \tag{17}$$

Where D_L and D_G are diffusivity constants for water and air, denoted liquid and gas. $D_L = 1.9 \times 10^{-9}m^2/s$ and $D_G = 1.98 \times 10^{-5}m^2/s$. The equations show that the diffusivity is highly dependent on the proportion of water and air as the ratio of $D_G/D_L \approx 10000$. The transport equation for the oxygen can then be written as a function of the VOF constant α:

$$\frac{\partial O_2}{\partial t} + \nabla \cdot (uO_2) = \nabla(D\nabla O_2) \tag{18}$$

The interface between water and air means there is a gradient in the diffusion. At an elevation in the

interface, there is a condition that needs to be fulfilled where the diffusion is equal. It can be written as:

$$D^l \nabla O_2 = D^g \nabla O_2 \tag{19}$$

Schmidt's number is a dimensionless quantity that lends parallels to theorems of heat transfer. Schmidt's number characterizes the transfer of mass between mediums. The number is a ratio between the viscous diffusion rate and mass diffusion rate (Bergman et al., 2011). This quantity is used for obtaining the values for D_G and D_L for the analysis.

$$Sc = \frac{\text{momentum diffusivity}}{\text{mass diffusivity}} = \frac{\nu}{D} \tag{20}$$

where D is the resultant diffusion constant acquired from equation 19.
Henry's law is a gas law that shows the proportionality between the gas diffused in a liquid and the pressure in the system. This means as the pressure of the system increases, air will diffuse into the water from the atmosphere above the fluid. The equation for diffusion as presented by Sander (2015) can be written as a temperature dependent equation.

$$He = He^\theta (T^\theta) \times RT \tag{21}$$

where He is a dimensionless number and He^θ is a coefficient from room temperature at $T = 298.15K$. R is the ideal gas constant for calculating the volume of gas taken by a mol of a chemical compound. Combining the oxygen transport equation together with the VOF and diffusion constant equations, the equation formed as shown by Yin et al. (2021) can be written as:

$$\frac{\partial O_2}{\partial t} + \nabla \cdot (uO_2) = \nabla(D\nabla O_2) + \nabla \left[\left[\frac{O_2(He-1)}{\alpha He + (1-\alpha)} \right] \nabla \alpha \right] \tag{22}$$

The transport equation establishes the convection of oxygen between water and air at the interface layer. For the study, the Henry constant is set to 0.01, which is the ratio of oxygen in the water to oxygen in the air.

2.1.6   Flow velocity

The velocity of the flow in the simulation is a relevant parameter that needs to be measured. A component of the velocity is the radial velocity, which is important for determining the water flow towards the outlet of the tank. The velocities become apparent when the flow field of each tank settles to equilibrium. A particle going in a clockwise pattern will have varying velocities in X and Y direction, so the radial velocity can be defined as a function of the coordinate. This velocity component will be used to compare the fluid flow in the tanks with different geometries and determine the effectiveness

of water recirculation in the tanks.

$$U_\theta(x,y,z) = U_y(t)\frac{x}{\sqrt{x^2+y^2}} - U_x(t)\frac{y}{\sqrt{x^2+y^2}} \tag{23}$$

The equation outputs the resultant velocity component of a fluid particle and its velocity towards the outlet in the center of the tank. A high tangential velocity means the water has a high recirculation velocity. This velocity is dependent on the cartesian coordinate (x,y) in the domain and the velocity of the flow U_x, U_y.

3   Numerical setup

This section explains the setup of the simulations and the data extraction method that are compared in the results section.

3.1   OpenFOAM and solver

OpenFOAM is an open-source CFD software used to create and simulate environments interaction with fluid. It is adaptive such that custom solvers can be compiled to solve numerical operations in loops to approximate solutions to fluid phenomenons. The solver is based upon a hierarchy of folders defining the initial conditions and boundaries for the simulation. The simulation operates on the governing equations of fluid mechanics and auxiliary equations for the computational setup, such as the Courant number. A simulation is created using a hierarchy of folders that control aspects of the simulation.

```
Simulation case folder
├── 0
│   ├── alpha.water
│   ├── C
│   ├── Ctest
│   ├── epsilon
│   ├── k
│   ├── nut
│   ├── omega
│   └── U
├── Constant
│   ├── dynamicMeshDict
│   ├── g
│   ├── RASProperties
│   ├── transportProperties
│   └── turbulenceProperties
└── System
    ├── blockMeshDict
    ├── controlDict
    ├── fvSchemes
    ├── fvSolutions
    ├── ProbesDict
    ├── SnappyHexMeshDict
    └── topoSetDict
```
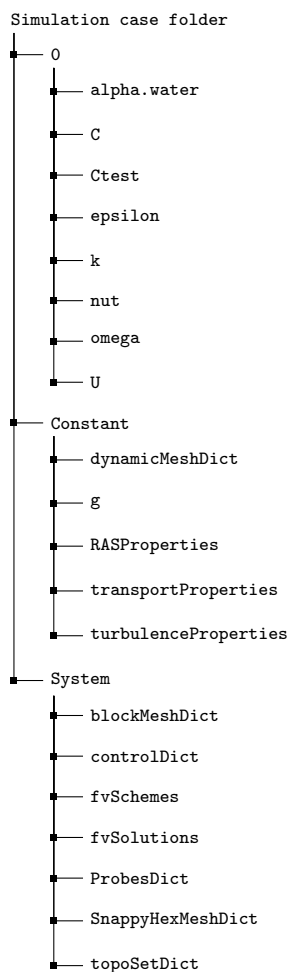
Figure 3.1: Hierarchy of the interTurbO2Foam solver

The diagram in 3.1 shows the folder structure for OpenFOAM simulation. Each folder contains properties that compose the simulation case. Most of the files are composed of text scripts and plain text

files that specify the properties of the simulation.

The **0** folder contains the initial conditions and boundary conditions for the simulation. The files contain the flow fields of the flow quantities that are investigated in the study. *C* are the oxygen concentration scalar fields. The velocity field is represented by *U*, and the *alpha.water* file represents the proportion of fluid within a cell, which is key for the VOF method.

The **Constant** folder defines the physical properties of the simulation model. Parameters such as gravitational acceleration, fluid properties and turbulence properties that are used in the present model.

The **System** folder contains the numerical settings such has discretization schemes and algorithms to solve linear equation systems for the simulation. Parameters such as time steps, write intervals, start and end times can be defined based on the simulation in the directory.

3.2   Models & Probes

The models used for the simulations have different designs for the water tank shape. The choice of geometries for the study are discussed in the end of the section. Overall the geometrical features are kept identical and in the same positions for all cases include:

- The inlet nozzle heights and diameter

- The outlet height and diameter

- The sensor probe

- The maximum tank width/diameter and height

(a) water tank dimensions (Wall removed for better visibility)   **(b)** Detailed view of inlet
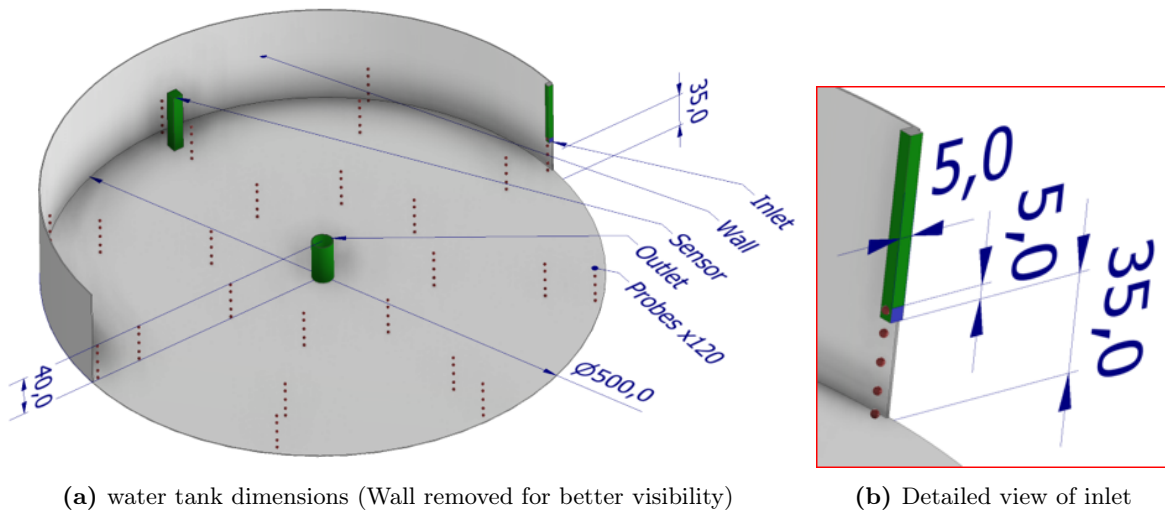
Figure 3.2: Dimensions (cm) for circular water tank model for circular case.

The water tank in figure 3.2 is the first case with a circular outer geometry. In the center marked green, there is an overflow outlet which stops water depth from increasing higher than 40cm without removing water from the system. The outlet is a PVC pipe of $20cm$ diameter. The pipe marked green on the wall is the square inlet with a $0.05m \times 0.05m$ inlet region. The other three cases have a cube footprint with filleted edges of different diameters. These fillets are the core difference between the designs in the study. The red dots shown in figure 3.2 show the spatial placement of the probe locations where pointwise data is measured.

3.2.1   Selection of probe points & nomenclature

The flow data to be gathered are collected at specific points of the water tanks which can then be compared across the different cases based on their position relative to the listed tank features. A single probe point is used to measure time evolutions for the different field variables. The variables in focus for the present study are the measurements of dissolved oxygen concentration and the flow velocities at the different probes. These can then be compared across the different cases to investigate the aquatic conditions within the tanks. The probes are also used for validation study by comparing with the experimental data. Due to the number of probes used in the study, it is important to clarify the probe locations.
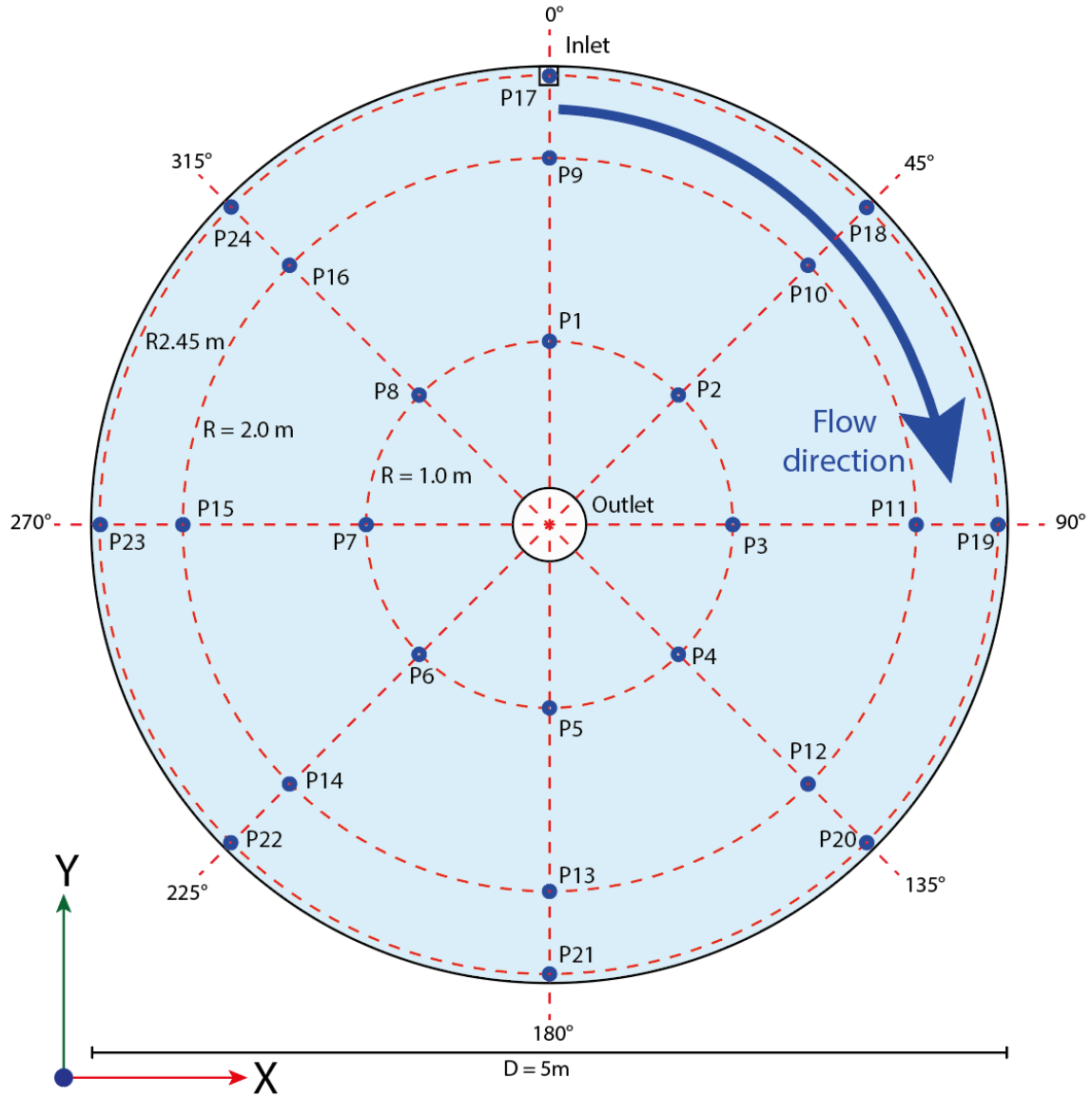
Figure 3.3: 5.0m diameter circular water tank model for Case 1

Figure 3.3 shows the horizontal plane view of the circular water tank design for Case 1. The points in the diagram are probes for a single plane layer. The number of probes and their locations are selected based on point measurements from experimental data obtained by *Jeju Ocean and Fisheries Research Institute of Korea* in Yin et al. (2021). The shape of the circular water tank has the smallest flow domain to compare across several cases, therefore the probe locations are confined within the geometry to prevent extrapolation of data with the square geometries that have extended boundaries. A 3D-polar coordinate system is used to define a probe point P at (r, θ). The radius r is the distance from the center of the overflow pipe (outlet) to the probe location. Three different radii have been selected at $R = 1.00m$, $R = 2.00m$ and $R = 2.45m$ for the study. The radii are shown as dotted red

circles in figure 3.3. θ is the resultant angle to the coordinate from the axis between the inlet and outlet in the clockwise direction. As shown, the angle between the outlet-inlet line is the angle origin at 0 °in the same direction as the inlet flow. A 45° interval between coordinates have been selected for the study, which means there are eight points around a single radius. Each of the 24 points in the plane record measurements at five different elevations of the tank from bottom to top.

The five plane heights selected are $0.02m$ $0.1m$, $0.2m$,$0.3m$ and $0.38m$ from the fish tank bottom respectively. The planes have approximately $0.10m$ spacing for the probe locations, except for the top and bottom planes. The top plane is offset $0.02m$ below the free surface of the water and the lowest plane is offset $0.02m$ above the tank bottom to avoid the measurements uncertainty close to the bottom and the water surface. The five heights allow for comparison of field variables in a point P as a function of the height. For 24 points with five heights, that gives 120 probes in total.

The probes have been assigned a number as shown in figure 3.3. It is shown that P1 to P8 are defined at $R = 1.0m, \theta = 0°$, increasing number in the clockwise direction. The next radius $R = 2.0m$ carries on the pattern with P9 to P16. $R = 2.45m$ contains the last range of P17 to P24.
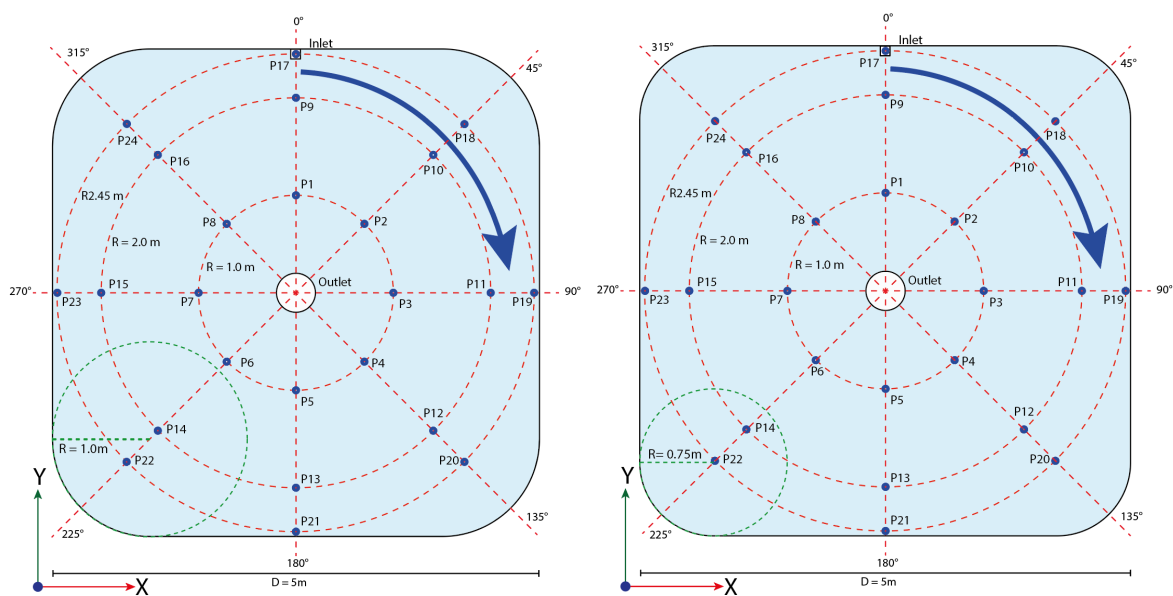
(a) Plane view of Case 2 water tank design with 2.0m diameter corner fillet

(b) Plan view of Case 3 water tank design with 1.5m diameter corner fillet
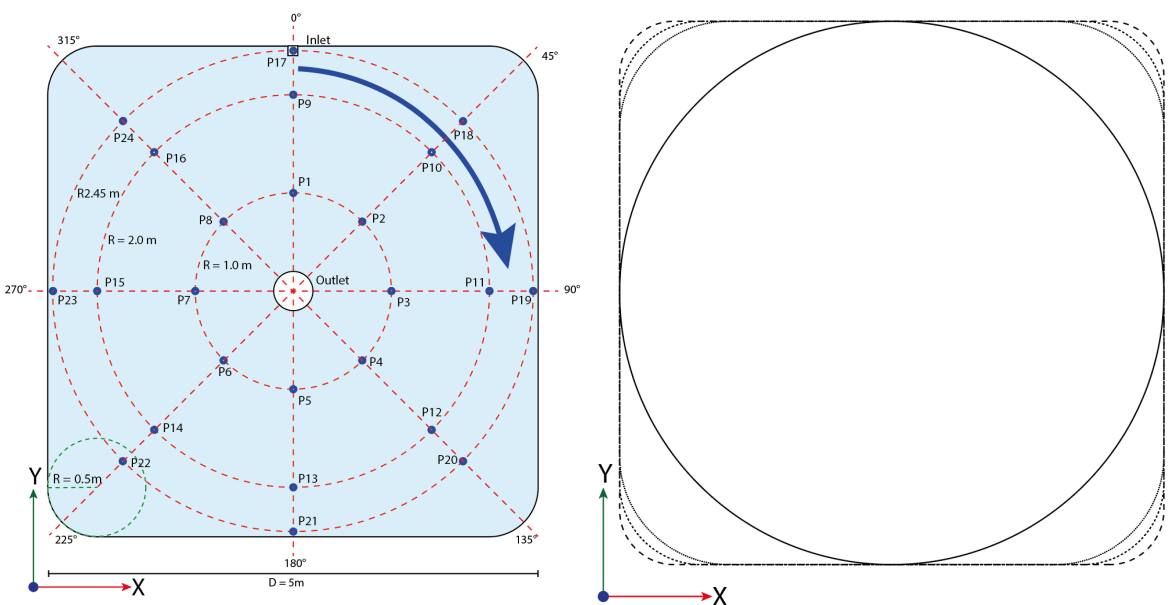
(c) Plane view of Case 4 water tank design with 1.0m diameter corner fillet

(d) Plane view of all water tank design outlines combined

Figure 3.4: Overview and comparison of top plane views of water tank cases 2-4

Figure 3.4 shows the tank designs in cases 2,3 and 4 and their footprints from top-down view. A combined layout of the plane views are shown for comparison of the geometries between different cases in figure 3.4d. The probe locations in the subfigures are identical as shown in figure 3.3.

The selection of water tank geometries were based on generic shapes and set fillet diameter to tank

width ratio; d/D. The circular tank in Case 1 is a reference to compare with square tank geometries. The square tanks with the sharpest, (i.e. smallest) fillet is given a fillet diameter of 0.2 relative to the tank width. This boundary is chosen because a nearly complete square tank would severely impact the momentum of the fluid in the tank. Increments in the d/D ratio towards a circular case where $d/D = 1.0$ would be preferred. However due to the computing cost, the number of investigated cases is limited. The d/D ratio is limited to 0.4 for square tank, because larger ratio defeats the purpose of square tank geometries when the shape is nearly circular. In practical terms, a d/D ratio of 0.9 for instance would mean there would be 0.5m of straight wall section, which is nearly circular by itself. The geometrical information of the water tank of the investigated cases is listed in table 3.1.

3.2.2   Design summary

Tank geometry	Corner diameter- d (m)	Overall width- D (m)	d/D ratio	Water capacity (m^3)
Case 1	5.0	5.0	1.0	7.84
Case 2	2.0	5.0	0.4	9.64
Case 3	1.5	5.0	0.3	9.79
Case 4	1.0	5.0	0.2	9.90

Table 3.1: Summary of geometry design features

3.3   Mesh

Meshing is an important step of solving discretized governing equations for the flow domain. It is a core process of the numerical setup which makes it possible to compute flow quantities in particular cells. The model as a single entity is segmented into a grid of cells, or lattice that make up the shape of the model.

Several geometries of meshes can be used and the resolutions of the mesh are important for producing accurate simulation results. Therefore the appropriate geometry and mesh density must be considered. The size of the mesh, i.e. number of discretized elements in the model affect the resolution of the results and computation time. A fine mesh can produce accurate results at the expense of computation time and vice versa. Therefore it is important to achieve a balance between the grid resolutions and the computational amount

The mesh can also be refined locally to yield more accurate results in areas of interest in the model. The main areas of interest are:

- The interface between the water and the air around the water surface

- Outer walls of the tank where velocity profile at the boundary layer is affected by the no-slip condition and there is a velocity gradient of the flow.
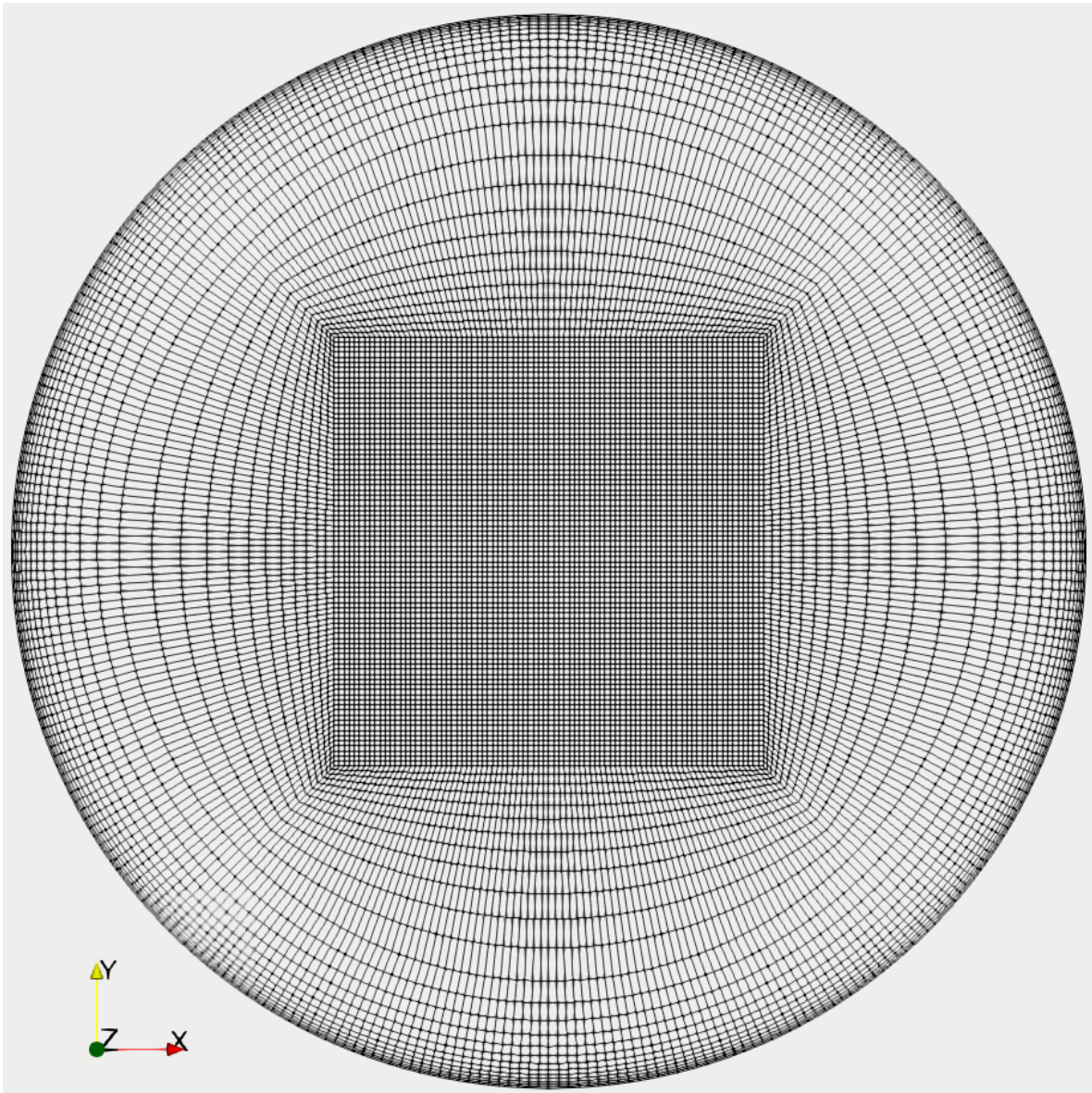
(a) water tank mesh from top-down view
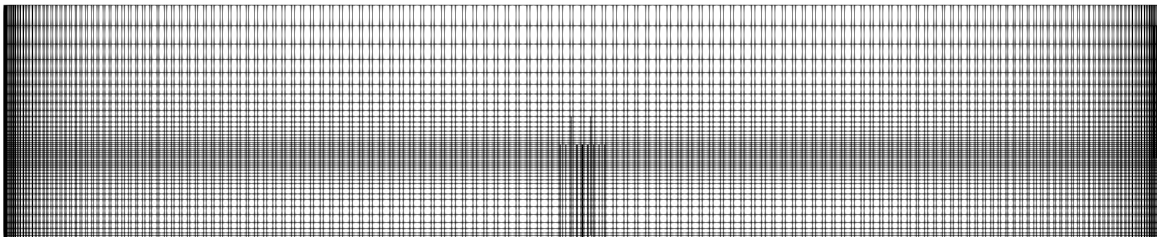
(b) Side view of mesh with visible mesh refinement

Figure 3.5: Images of mesh from circular geometry in Case 1

(a) water tank mesh from top-down view
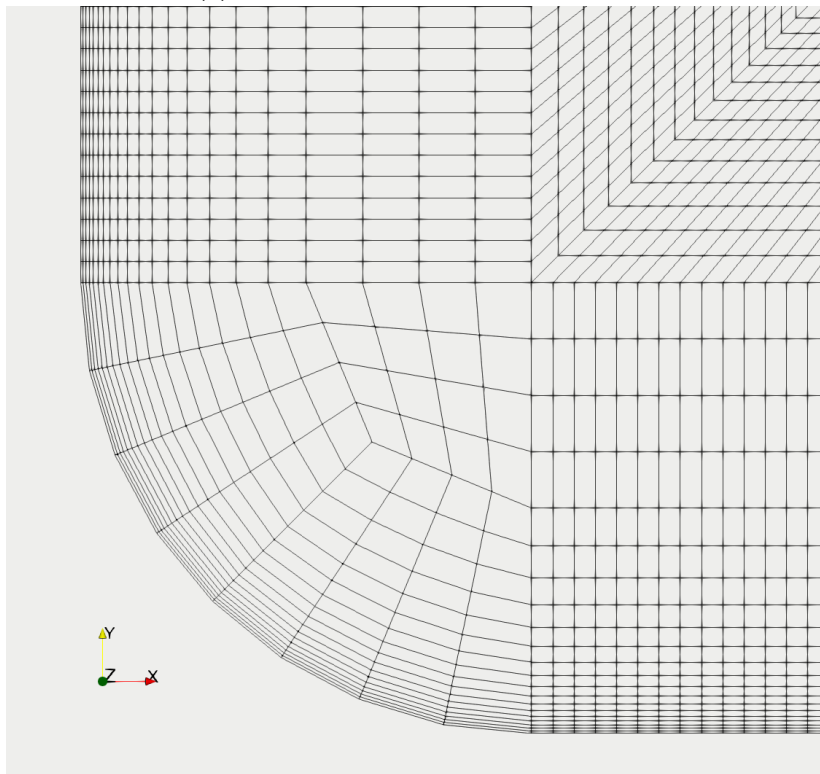
(b) water tank mesh at wall

Figure 3.6: Images of mesh from Case 3

The mesh for the computational setup is made using the mesh generation software **Gmsh**. Figure 3.5 shows the generated mesh of the circular water tank. The mesh is composed of quadrilateral elements to form a structured mesh. Figure 3.5b shows the refinement of the mesh at the interface layer. A high resolution of the grid at this height helps capture the transition between water and air for the flux of oxygen.

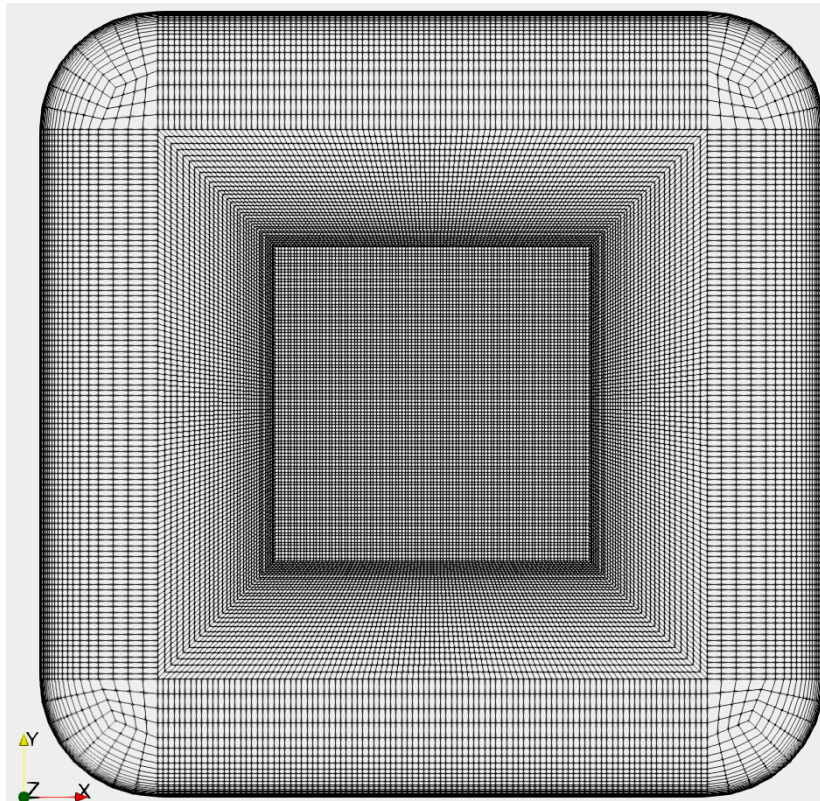Figure 3.6 shows the mesh for the model in Case 3. The mesh has been split such that the mesh retains its quadrilateral structure despite the rounded corners. The close view image in figure 3.6 shows the boundary layer mesh refinement. Looking at the mesh towards the wall, the width of the element decreases as it nears closer to the wall surface, which is used to capture the boundary layer velocity profile effectively. The refinement prevents estimating the profile across a coarse mesh.

3.3.1 Mesh data summary

To select an appropriate mesh resolution to achieve a balance between the accuracy and the computational amount, a mesh convergence study is performed in terms of the concentration of the dissolved oxygen. The table below shows the summary of the generated meshes that are used for the convergence study. Five meshes are used. There is an additional refined mesh for Case 1 used for convergence study.

Water tank study	Elements	Nodes
Case 1- Coarse	646035	667185
Case 1- Refined	679296	703092
Case 2	1778669	1824200
Case 3	1778612	1824172
Case 4	1778847	1824456

Table 3.2: Summary of water tank geometries mesh

3.4 Initial conditions & boundary conditions

The initial conditions are based on the study by Yin et al. (2021), which are listed in table 3.3.

		p	O_2
Inlet	$u \cdot n = 2.12 m/s$	$\frac{\partial p}{\partial n}$	$\nabla O_2 \cdot n = 0.00827 kg/m^3$
Outlet	$\frac{\partial u}{\partial n} = 0$	$p = 0$	$\frac{\partial O_2}{\partial n} = 0$
Walls, sensor and outlet cylinder	$u = 0 m/s$	$\frac{\partial p}{\partial n} = 0$	$\frac{\partial O_2}{\partial n} = 0$

Table 3.3: Boundary conditions as used by Yin et al. (2021)

Table 3.3 as a summary of boundary conditions can be written descriptively to convey their use in the numerical setup.

- At the inlet, a uniform flow using a fixed flow rate is prescribed with a mass of $Q = 15t/h$ and the flow velocities of $\vec{u} \cdot \vec{n} = 2.12 m/s$. $\vec{n}$ is the normal unit vector of the inlet face. The pressure is prescribed as zero gradient. A fixed oxygen concentration of $0.00827 kg/m^3$ is set at the inlet.

- At the outlet, the flow velocities are set as zero normal gradient and the pressure is set to be zero. Zero normal gradient is used for the oxygen concentration.

- At the walls, the flow velocity is set to be zero and the pressure is set to be zero. Zero normal gradient is set to the oxygen concentration at the walls.

3.5 Post-processing

The simulations are post-processed in an open-source visualization tool, where the flow field variables are obtained for comparison between the cases. The ParaView software application can load the time step results from OpenFOAM into the GUI for processing. ParaView allows for visual results to be extracted for comparison, as well as point cell data that can be exported to spreadsheet data. The collection of raw spreadsheet data can then be loaded into MATLAB environment to process the data exports further. In short, the work process behind the post-processing can be summarized in three stages:

- Use ParaView software application to export renderings of slices and relevant images showing results clearly. Then export the point data containing relevant parameters for each time step.

- Import the collected spreadsheet data into MATLAB to write script manipulating arrays together to plot time-series of results at defined coordinates.

- Compare relevant data for points of interest.

4   Convergence study

In this section, a convergence study is conducted to determine the accuracy of the computational setup and mesh independence. The study investigates Case 1 simulation using two meshes of different sizes to compare their final solutions.

The dissolved oxygen content between the two simulations are compared to see the difference between their final solutions using the time data plots and bar charts. The time-dependent measurements are useful for showing the time-evolution of the dissolved oxygen towards a final steady state. The main advantage of time-history data is the final solution is supported by trend rather than an instantaneous final result. The difference between the results from the meshes can be plotted as the relative difference between the results. From this comparison, the simulations can be determined to which extent the final solution at $t = 3000s$ has converged.

A few selected probe points are used to show time-dependent measurements of oxygen concentration in the two meshes. It is of interest to obtain measurements of locations that yield results indicative of the equilibrium state of the water tank. The selection is important because some probe locations indicate the conditions of the computational setup than the flow field. For instance, a velocity measurement at a probe close to inlet only confirms the inlet velocity is correctly defined, rather than determining the steady state conditions of the domain.

The probe locations P7, P15 and P23 are chosen for the study as they are far away from the turbulent jet of the inlet. These points are found in the radii $R = 1.0m$, $R = 2.0m$ and $R = 2.45m$ respectively at the 270° axis.
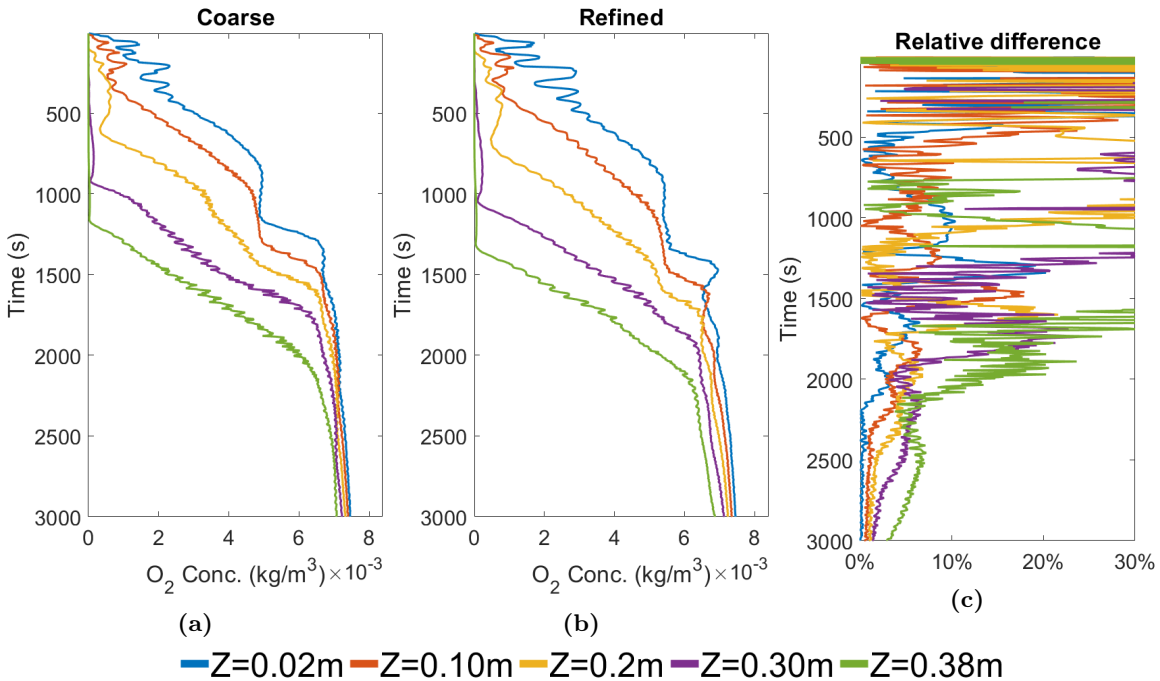
Figure 4.1: Concentration over time at P7 ($R = 1.0m$ and $\theta = 270$°) for different layers heights
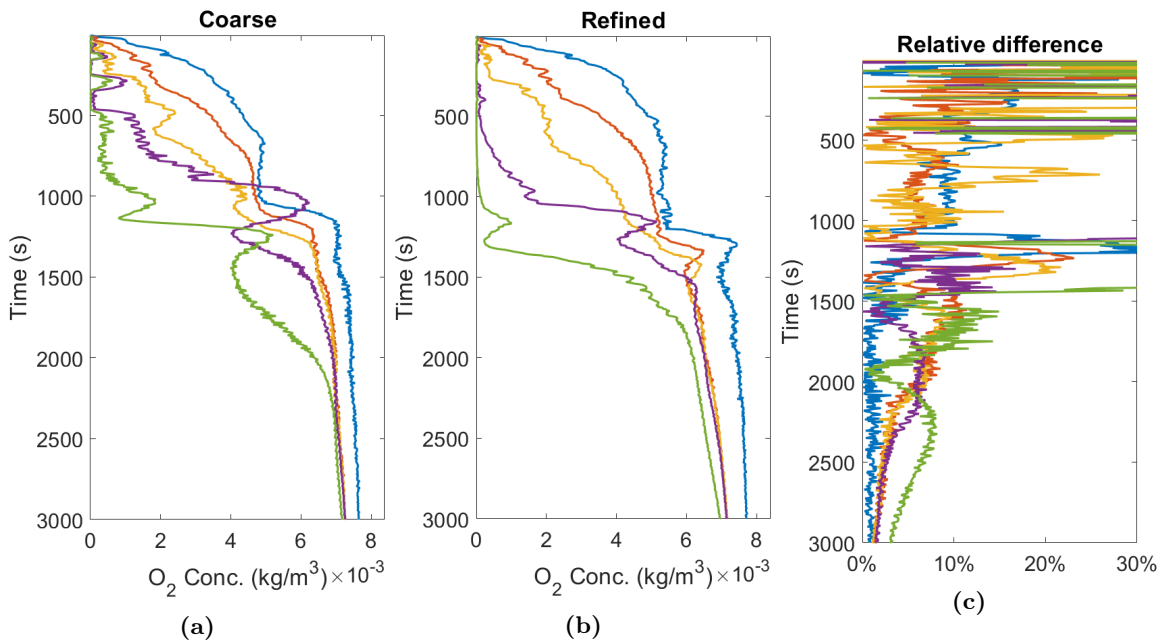
Figure 4.2: Concentration over time at P15 ($R = 2.0m$ and $\theta = 270°$) for different layers heights

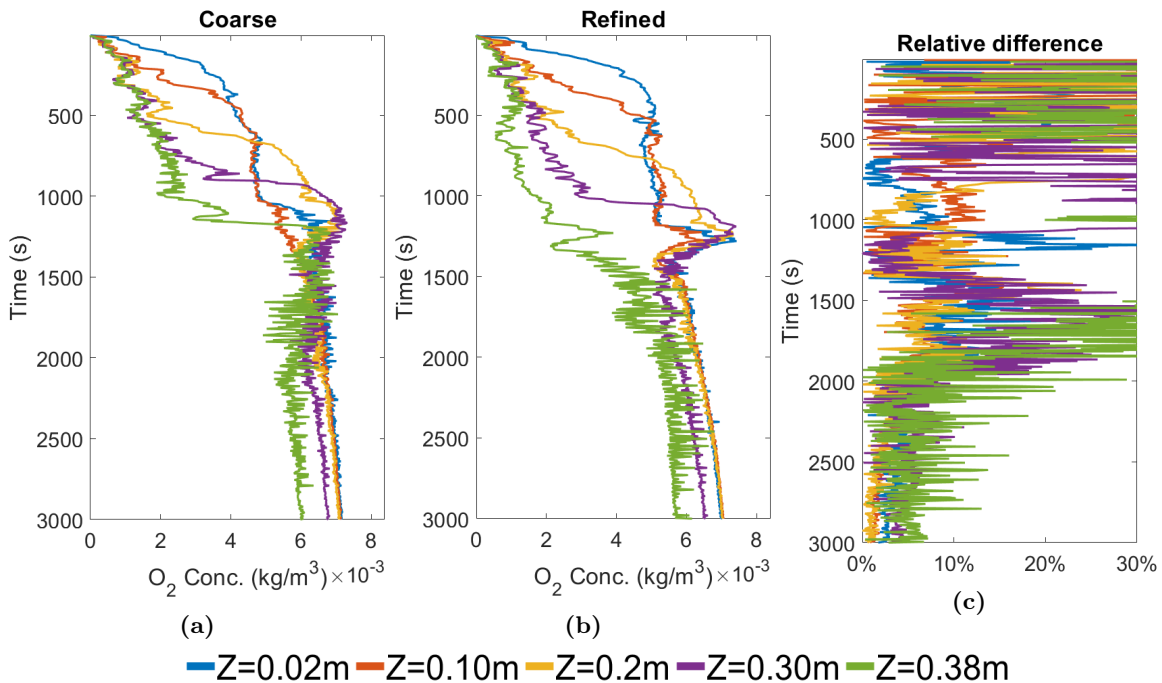**Figure 4.3:** Concentration over time at P23 ($R = 2.45m$ and $\theta = 270°$) for different layers heights

Figures 4.1-4.3 show the time-evolution of the measured dissolved oxygen concentration for the probes until $t = 3000s$. The results for each mesh is presented in separate plots. Each plot line represents the oxygen content of the probe at a specific layer height. The subfigures in **a)** show the development of

the oxygen concentration over time for the coarse mesh. The subfigures in **b)** show the time-evolution of the measured dissolved oxygen concentration for the refined mesh. The last subfigures in **c)** shows the relative difference between the results of the meshes.

Figure 4.1 shows that the point measurement at $Z = 0.02m$ increases first followed by ascending layer height. This is due to the rising water level of the tank registering volume of water with dissolved oxygen. It can be seen that the water reaches $Z = 0.38m$ at approximately $t = 1200s$, causing the water with the dissolved oxygen to rise expectedly. From this time onward the model converges towards steady state at $t = 3000s$.

Figures 4.1a and 4.1b show clear trend towards a steady oxygen concentration occurring at $t = 2000s$ and further equalize towards $t = 3000s$. Figure 4.1c shows the result difference between the meshes, where the concentration stabilizes at $t = 2500$. The concentration of each measurement is nearly equal across all heights towards the end time. The final oxygen content ranges at $0.007 - 0.0077kg/m^3$ for all layer heights at P7. In figure 4.1b. The result range is slightly larger, where the probes have a lower recorded oxygen concentration. This difference is visible in figure 4.1c where the maximum difference is shown for P7 probe at $Z = 0.38m$. An important result from this comparison shows that the difference increases with the increasing Z height of the probe measurement. $Z = 0.38m$ probe height exhibits the largest concentration difference of 3%, whereas $Z = 0.02m$ is near identical for both meshes. It is evident that the difference for $Z = 0.38m$ is still declining at $t = 3000s$, which means extended simulation period could be conducted to see the final difference in oxygen content.

Figure 4.2 shows the same trends as seen in the time-evolution plots for P7. At this radius, the results deviate less than seen in figure 4.1. The concentration range difference in figure 4.2c is increased to show the two emerging peaks for $Z = 0.3m$ and $Z = 0.38m$. The peaks rapidly emerge and disappear in the time steps before reaching a steady state with measured differences. The relative difference in oxygen concentration between the meshes is 3.3% for the surface layer.

Figure 4.3 Shows the oxygen concentration measured at the largest radius of the tank at $R = 2.45m$. The plots for P23 are similar to P15 in terms of progression towards the final steady state. The main characteristic difference is the fluctuation in the $Z = 0.38m$ layer. This turbulent convection of oxygen is expected as the inlet face intersects with the layer. Despite the distortion in results difference, the solution converges towards a relative difference of 7.2% considering the largest peak difference at $t = 3000s$.

In summary the time history plots show that a steady state solution for the dissolved oxygen content. The relative difference for the final oxygen concentration in the selected probes is 3.6% for the two meshes. The oxygen content difference between the cases diminish with time and decline further with longer time step duration above $t = 3000s$.
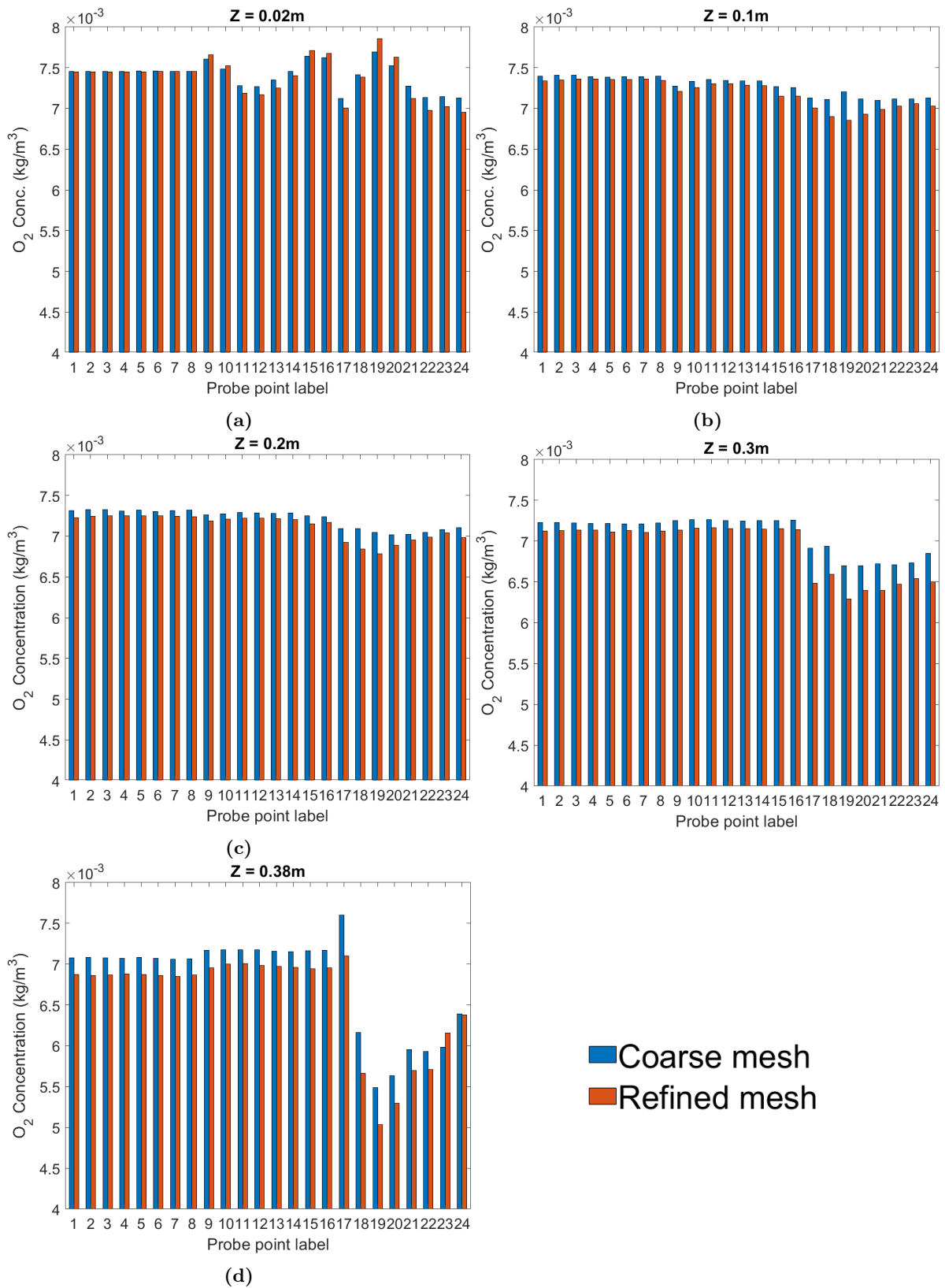
Figure 4.4: Final steady state oxygen concentration between meshes for different heights at $t = 3000s$

The bar diagrams in figure 4.4 show the final oxygen concentration at $t = 3000s$ for each individual probe between the coarse and refined mesh. The plots are split into subfigures according to their layer height. All 120 measurement points between each study are compared against each other for the coarse and refined mesh. It is evident that most of the oxygen concentration measurements are lower for the refined mesh. However the solution can still be regarded as converged based on the relative difference between the simulations. The mesh can be refined further to get better results.

The bottom plane at $Z = 0.02m$ shows consistent concentration levels of approximately $7.4kg/m^3$ around the smallest radius from P1-P8 for both meshes. The difference between the meshes in these probe locations increase with ascending layer height.

At the radius $R = 2.0m$ from P9-P24 there is variation in the oxygen content along the clockwise direction of the flow. However, meshes are consistent with each other for these measurements.

In the last plot of figure 4.4, concentrations at $Z = 0.38m$ shows contrast in differences between the two cases from P17 to P22. The largest difference is seen at P19 where the concentration in the refined mesh is 8.3% lower than the coarse mesh. The oxygen concentration for all probes in the outer radius $R = 2.45m$ show larger gaps in the final results between the meshes. The outlier results can be traced to the turbulent wake of the inlet, which according to Reynolds number is calculated to $Re = 10600$. The solver seems to experience difficulty processing the oxygen convection in turbulent flow and is sensitive close to the water surface. As the turbulent kinetic energy dissipates, an increasing oxygen concentration is recorded in the probes for the outer radius.
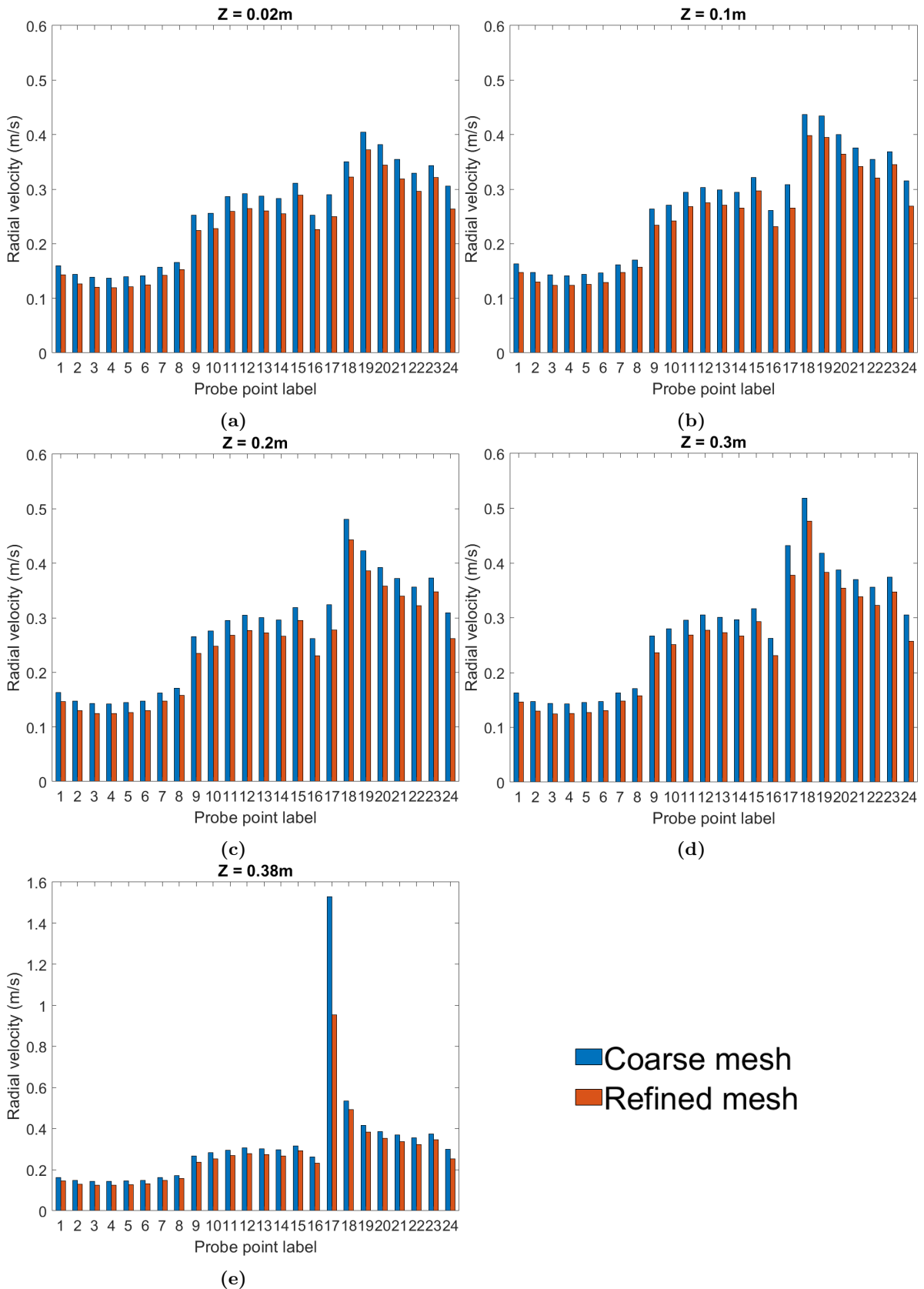
Figure 4.5: Steady state radial velocity between meshes for different heights at $t = 3000s$

Figure 4.5 shows the velocity of the water at time $t = 3000s$. The bar plots are divided according to their layer height as done with figure 4.4. The radial velocities measured show a divide between the measurements that are split by their radius. P1-P8, P9-P16 and P17-P24 show increased radial velocity with larger radius. The radial velocities are dependent on their radius position which is explained in the results and discussion section.

The radial velocity of P17 at $Z = 0.38m$ are measured at $1.53m/s$ and $0.95m/s$ for the coarse mesh and refined mesh respectively. The discrepancy between the two measured velocities show the results are sensitive to flow close to the inlet.

5   Validation study

In this section, the final solution of the solver is studied to determine the effectiveness of the computational setup. The approach of verifying the solution can be done by several methods, from creating analytical solutions and make comparisons with other solving algorithms or known solutions. Validation on the contrary draws correlation directly between numerical and experimental results.

The experimental data presented in the section is sourced from a water tank with the same geometry and domain as Case 1; A 5m diameter circular water tank with 0.40m water depth. The data consists of point measurements of oxygen concentration in the tank, in accordance to probes in figure 3.3. For this validation study, the data from the simulation is extracted at the same coordinate where the point measurements were conducted in the experimental trial. Three layers are used in the data acquisition for $Z = 0.1m$, $Z = 0.2m$ and $Z = 0.39m$.
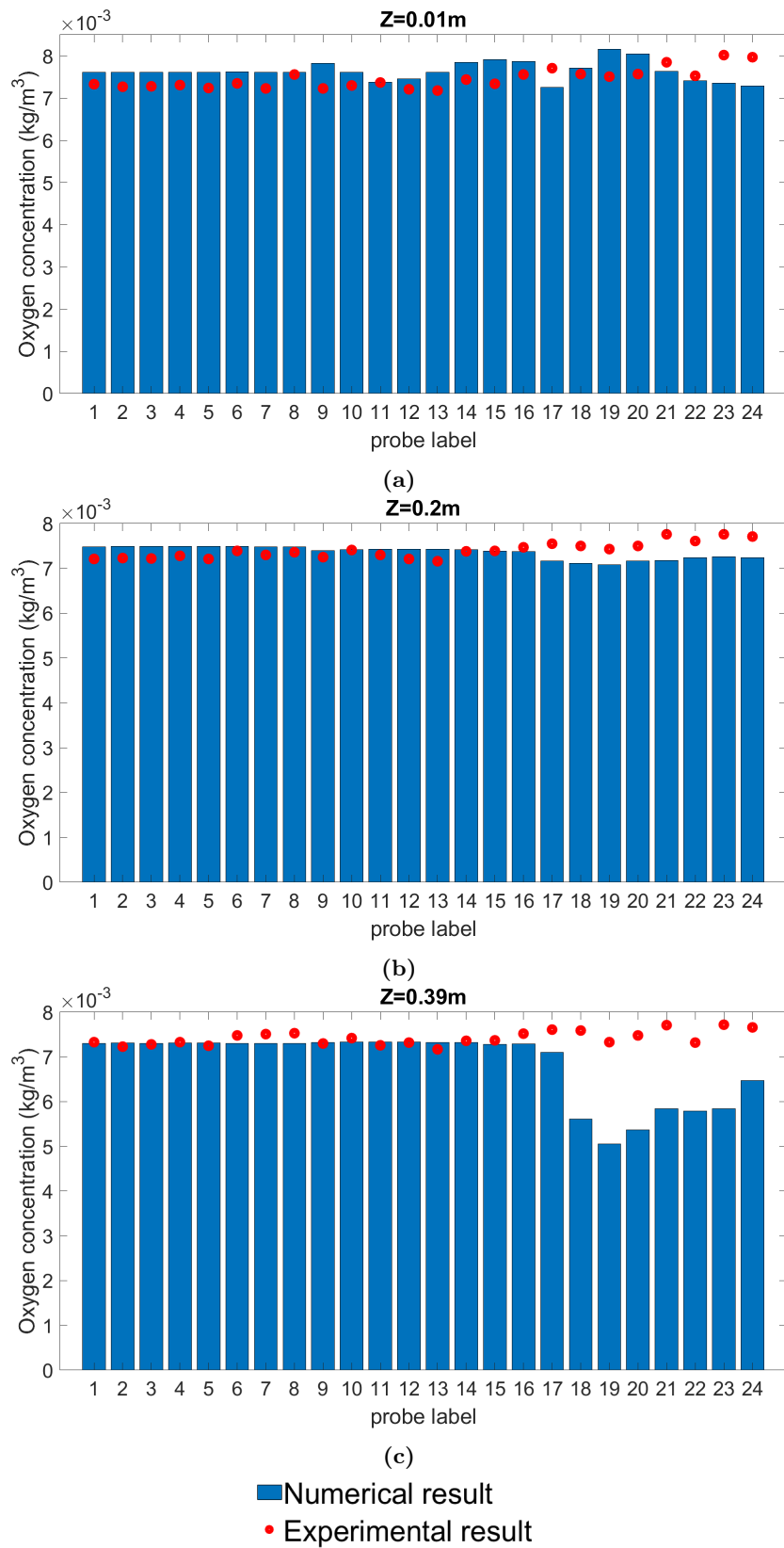
Figure 5.1: Case 1 comparison between experimental data and numerical result for different layers.

Figure 5.1 shows the comparison of oxygen concentration between experimental and numerical results. For this study the results obtained from using the refined mesh in the convergence study is used for comparison in the validation study.

The red data points show the experimental results of oxygen concentration at the probe points. It is evident the concentrations vary in the range of $0.007 - 0.008 kg/m^3$ across all layers. The maximum error between the results is 9.2% for figure 5.1a and 8.1% for figure 5.1b. The largest deviation for figure 5.1c is evident for probes P17-P24. These probes which are all located at radius $R = 2.45m$ show there is a systematic deviation in the numerical result. The deviation can be attributed to the turbulent wake of the inlet being carried around the walls in the tank and close to the water surface. The largest difference for the top layer is 45% deviation from the experimental result. When disregarding these anomalies, the points P1-P16 have a maximum difference of 3%.

The results of the validation study show that the final solution mostly agrees with the experimental data. It should be noted that the numerical result may still be converging towards the final equilibrium. Oxygen concentration is gradually increasing over time as shown in the figures 4.1-4.3. Comparing these results to a system that has had a longer time to fully saturate may be a source of error for the gap in P17-P24 in figure 5.1c. Despite the fluid flow reaching equilibrium, the scalar field of oxygen is still saturating slowly. To obtain the true saturation of the water tank, the number of time steps simulated should be increased. The computational cost of calculating extra time steps coupled with the slow rate of saturation would not yield more relevant information as 113 of the 120 probes have shown close predictions with the experimental data.

6   Results and discussion

The results gathered from the CFD simulations are presented in this section with discussion regarding the results. The results are shown using visualizations and plots exported from ParaView and MAT-LAB. The visuals include cross sections of horizontal planes to show the distribution of field variables in the simulations. The plots show field variables extracted from the probe locations plotted over time. Each case is individually presented and discussed before they are directly compared in the end of the section. The section of each case presents the visual results before presenting plots relevant for the flow and dissolved oxygen transport in the tanks.

6.1   Case 1: Cylindrical water tank geometry (d=5.0m)

Figure 6.1 shows the equilibrium oxygen concentrations at the layer heights $Z = 0.02m$, $Z = 0.2m$ and $Z = 0.38m$ from left to right. These selected layer heights are the same for every case presented in the subsections. Each respective layer presented in the sections and are referred to as bottom, middle and surface layers.

(a) $Z = 0.02m$　　　　**(b)** $Z = 0.20m$　　　　**(c)** $Z = 0.38m$

Oxygen concentration (kg/m³)

5.0e-03 0.0052 0.0054 0.0056 0.0058 0.006 0.0062 0.0064 0.0066 0.0068 0.007 0.0072 0.0074 0.0076 0.0078 0.008 8.3e-03
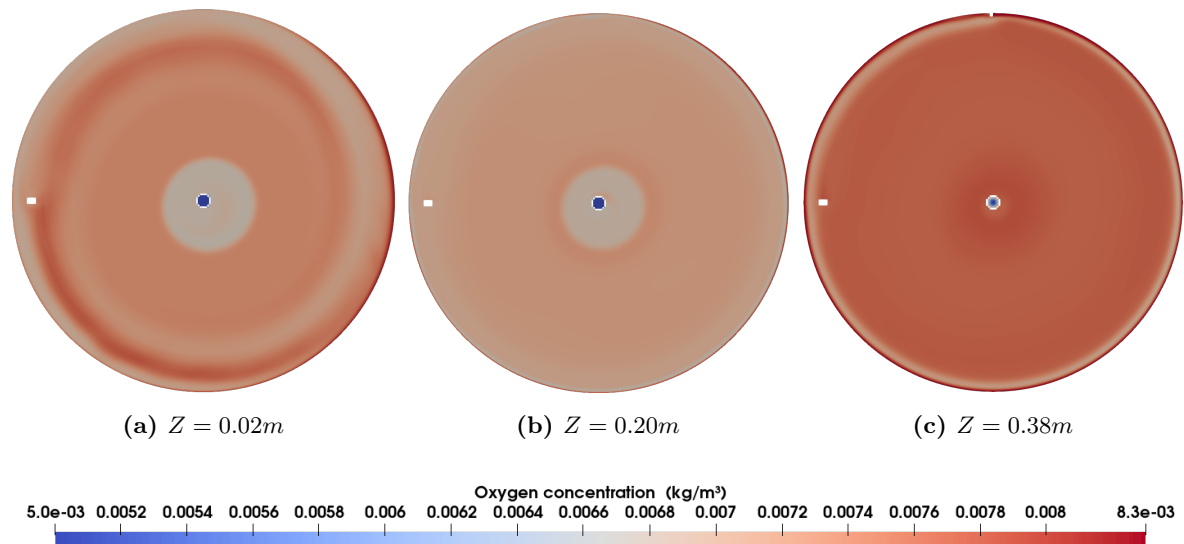
Figure 6.1: Oxygen concentration at $t = 3000s$ for different Z-layers of Case 1

(a) $Z = 0.02m$ **(b)** $Z = 0.20m$ **(c)** $Z = 0.38m$
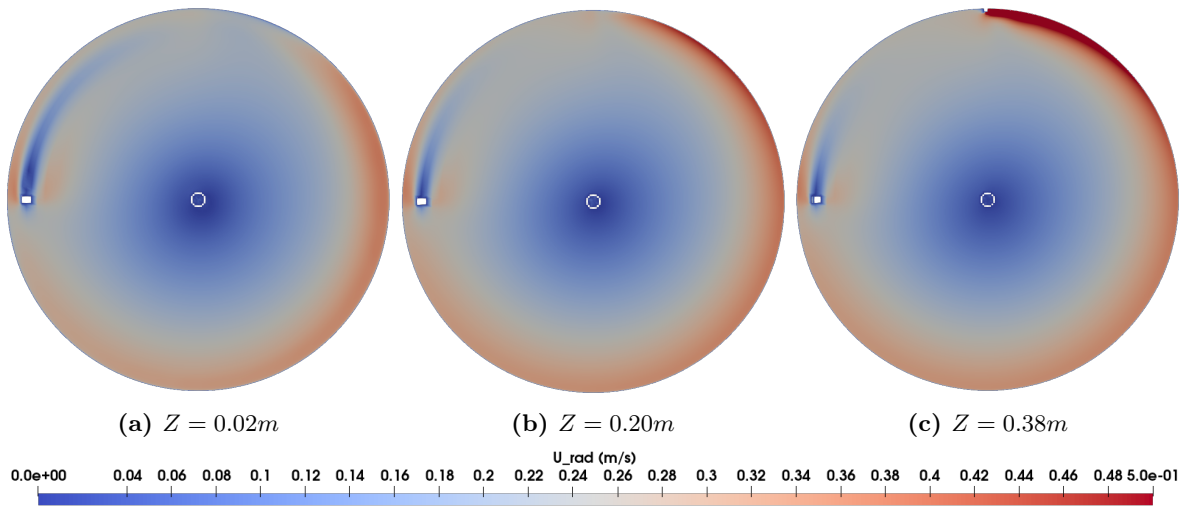
Figure 6.2: Radial velocity at $t = 3000s$ for different Z-layers of Case 1

The figure shows oxygen concentration varies at the bottom plane, with the middle and surface layers showing uniform distribution with rotational symmetry of oxygen saturation in each slice. The center of the tank shows a circular region with a visible drop in oxygen concentration, which indicates a stagnant region where the oxygen is not convected towards the center. The surface layer does not show the same stagnant region near the outlet as seen in figure 6.6a or 6.6c. This is due to the elevation of the inlet flow supplying oxygenated water at the surface near the free surface of the water.

Figure 6.2 shows the radial velocity of the horizontal planes with a gradually declining velocity towards the center of the tank. This phenomenon is expected as the fluid in a thin volume of water in a horizontal layer cannot physically move towards the center with constant velocity. The radial velocity in the planes shows some extent of rotational symmetry. The features of the tank affecting the velocity and the rotational symmetry are the flow inlet and probe sensor. The inlet injects water, which then forces the fluid to disperse radially as it is interacting with fluid in the tank.

Overall the velocities are nearly uniform over all the layers, which indicates a linear free stream velocity profile. It is evident that the radial velocity by the inlet is much higher than the legend's maximum limit of $0.50m/s$. There is a flow velocity decrease in the wake region behind the sensor due to the wake flow caused by the sensor, which is a common sight for all four cases.
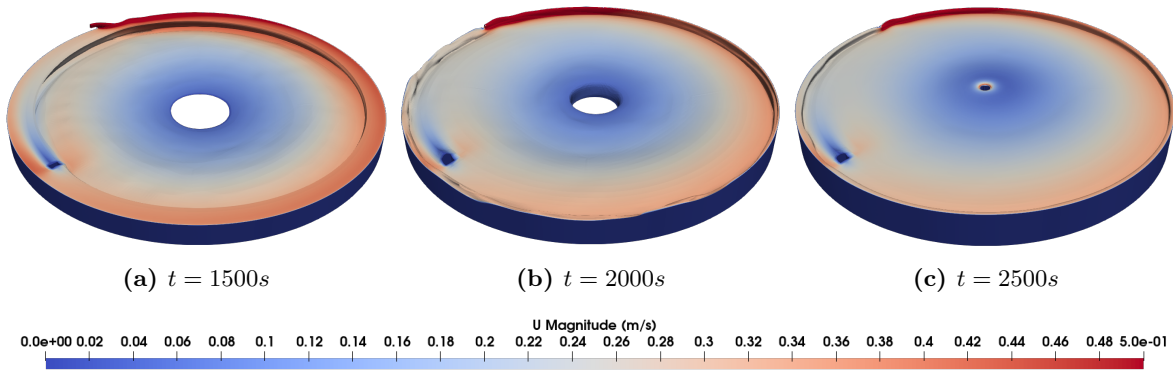
(a) $t = 1500s$ **(b)** $t = 2000s$ **(c)** $t = 2500s$

Figure 6.3: Oxygen distribution above $0.0050kg/m^3$ over time intervals t of Case 1

Figure 6.3 show the isosurfaces of the fluid domain where oxygen concentrations are above a set threshold criteria. The legend color of the isosurfaces are represented by the velocity magnitude of the fluid, which has a range of $0 - 0.5m/s$. Three figures are shown where the visible surfaces contain oxygen content equal or higher than $0.0050kg/m^3$. Any region of the tank with less oxygen content is therefore rendered invisible. The figures shows the progression of the oxygen transport in the tank over a selection of time intervals while it fills with water. It can be seen that the oxygen distribution progressively propagates towards the center of the tank and approaches equilibrium at $t = 2000s$.

The *clips* exported from ParaView show that most of the tank is saturated with respect to the threshold. It is important to mention the positioning of the view, which points toward the 225° axis. The inlet flow is more visible in equivalent figures for the other cases. This view is kept same for each case showing these clips.

(a) Above $0.0070kg/m^3$ **(b)** Above $0.0073kg/m^3$ **(c)** Above $0.0074kg/m^3$

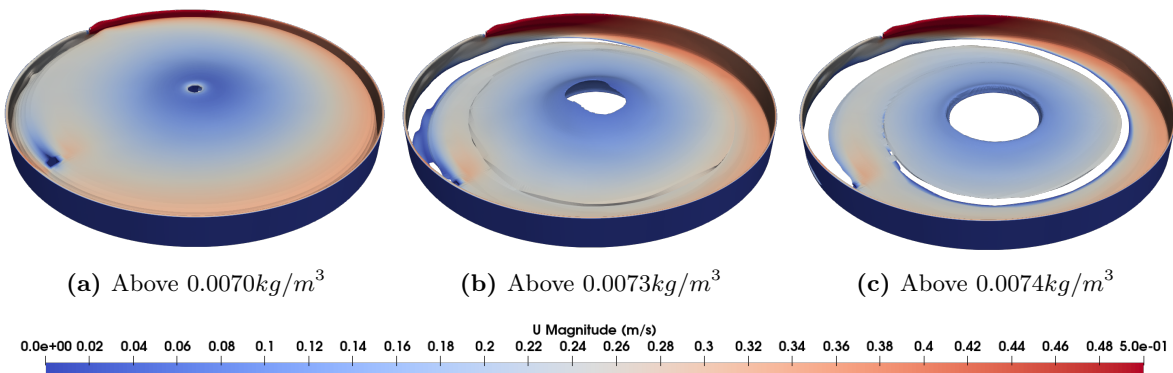**Figure 6.4:** Oxygen distribution isosurfaces at $t = 3000s$ for different thresholds of Case 1

Figure 6.4 show the isosurfaces of the fluid domain where oxygen concentrations are above a set

threshold. The figures are pictured from the same time step where the criteria limits are increased from left to right. This creates a contrast between the concentrations of oxygen where higher concentrations are seen in smaller regions. The figures show most of the tank is saturated with oxygen concentration above $0.0070kg/m^3$. When the limit is slightly increased in subfigures 6.4b and 6.4c, the concentration stays high at the bottom and the walls. It is evident that the center of the tank has a dome-shaped region around the outlet where concentration is lower than the rest of the tank. Figure 6.4a shows the empty dome-shape region when looking from the underside of the tank. This characteristic is similar for every single simulation case. In summary, the concentration in the circular tank is evenly distributed and nearly as high as the inlet concentration of $0.00827kg/m^3$.

6.1.1   Radial velocity

Figure 6.5 shows the radial velocity of the fluid at the probe locations in the water tank. The plots are separated by their probe radius position. Figure 6.5a shows the radial velocity over time for probes P1-P8. Figure 6.5b shows measurements for P9-P16 and 6.5c shows the remaining measurements for P17-P24. Each of the eight probes in the separate radius have three measurement points for different heights. This gives a total of 24 plot lines in a single subfigure. The planes selected for the comparison are $Z = 0.02m$, $Z = 0.20m$ and $Z = 0.38m$ layers to prevent excessive overlap in the data presentation.
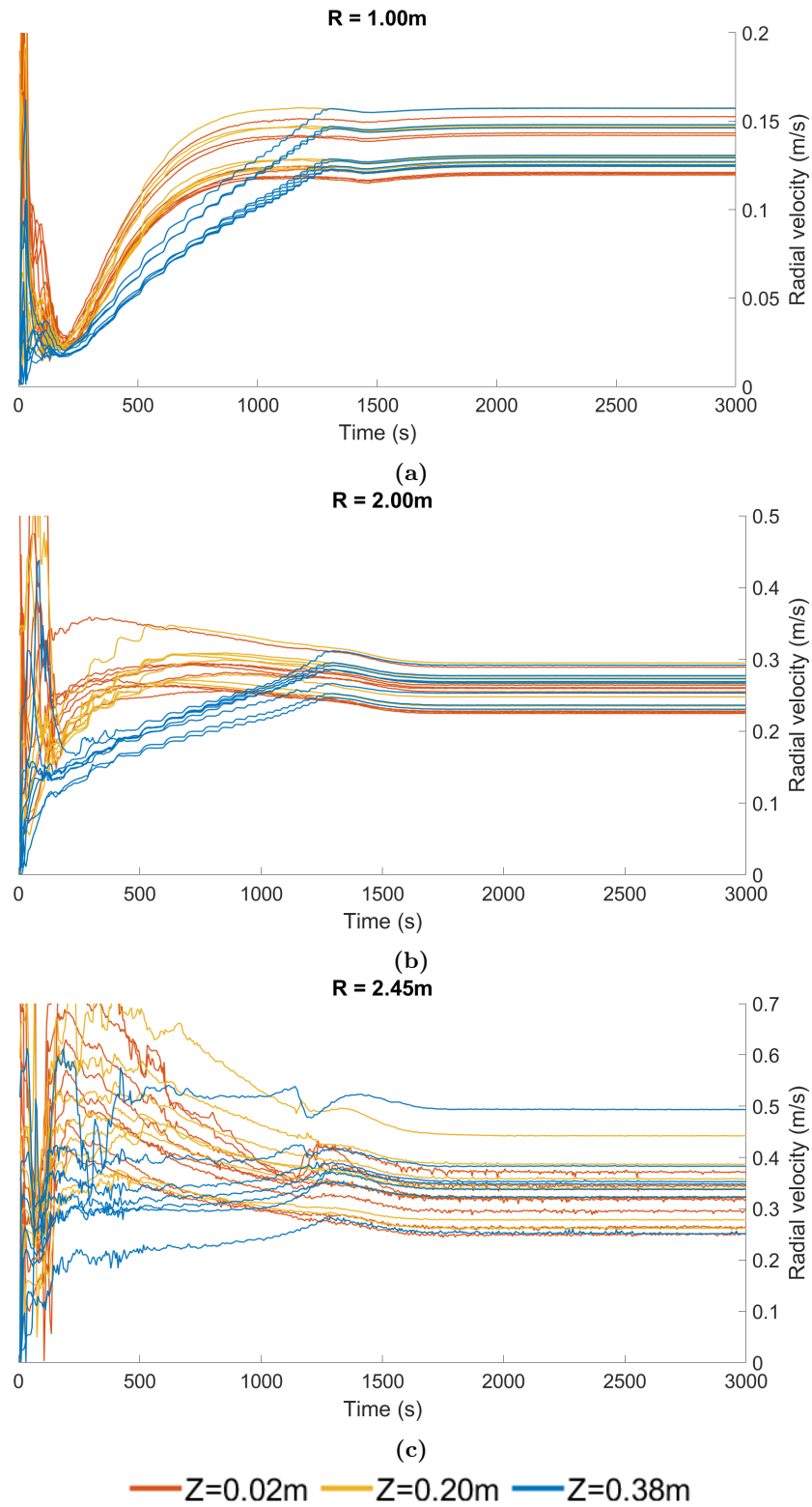
Figure 6.5: Radial velocity results at probes by radii for Case 1

41

A general observation from all the velocity figures is that the water flow reaches equilibrium at $t = 1500s$. This is evident as the flow becomes constant onwards with some fluctuation in the velocity. At the equilibrium state, the fluctuations of the flow velocity tend to be zero.

Despite the number of velocity measurements shown, the plots are useful for identifying the ranges of the flow field variables present in the domain and their position. Figure 6.5 shows the recorded velocities across the layers $Z = 0.20m$ to $Z = 0.38m$ have very similar velocity magnitudes in the vertical axis at each probe. This is shown by the overlapping lines between layers. The velocity near the water tank bottom at $Z = 0.02m$ is slightly decreased compared to the upper layers, which is due to the viscous effects by the bottom surface of the tank.

Figure 6.5a shows the velocity at the inner radius within the range $0.12 - 0.16m/s$. This range indicates a spiraling flow pattern where the radial velocity slows before the inlet. It should be highlighted there is a gap in the recorded velocity at $0.13 - 0.14m/s$ range which is not uniform with the rest of the probes.

Figure 6.5b shows the radial velocity range of $0.22 - 0.30m/s$. This range is larger, however the probes are evenly spread out, which indicates there is a uniform spiral motion in the fluid at the radius in the horizontal planes.

Figure 6.5c shows a larger range in the measured velocities for all the 24 measurement points at the outer radius. Most of the probes record a range of $0.28 - 0.40m/s$ with two probes going upwards to $0.0.45 - 0.50m/s$. These higher readings are expected due to the probes being in proximity of the inlet flow at the radius. As the water is injected into the domain, the water is forced in all three dimensions, including the radial direction. The velocity of the fluid coming out of the inlet is $2.12m/s$ but pushes some fluid aside that gives the local volume a higher velocity directly towards the inlet. This effect is visible in figure 6.2.

6.1.2   Oxygen concentration

Figure 6.6 shows the saturation of oxygen concentration for each layer in the water tank. Each subfigure shows the measurements of 24 probes which exist in their respective layer. The results for each layer are separated by their radius to show the distribution of oxygen in the regions of the tank from the center of the tank and outwards to the walls. The probes in a single layer are plotted together to give insight into the range of oxygen found within the layer height. If dissolved oxygen is perfectly distributed in the circular layer cross-section, the plot would show all results approaching the same concentration value.

(a)
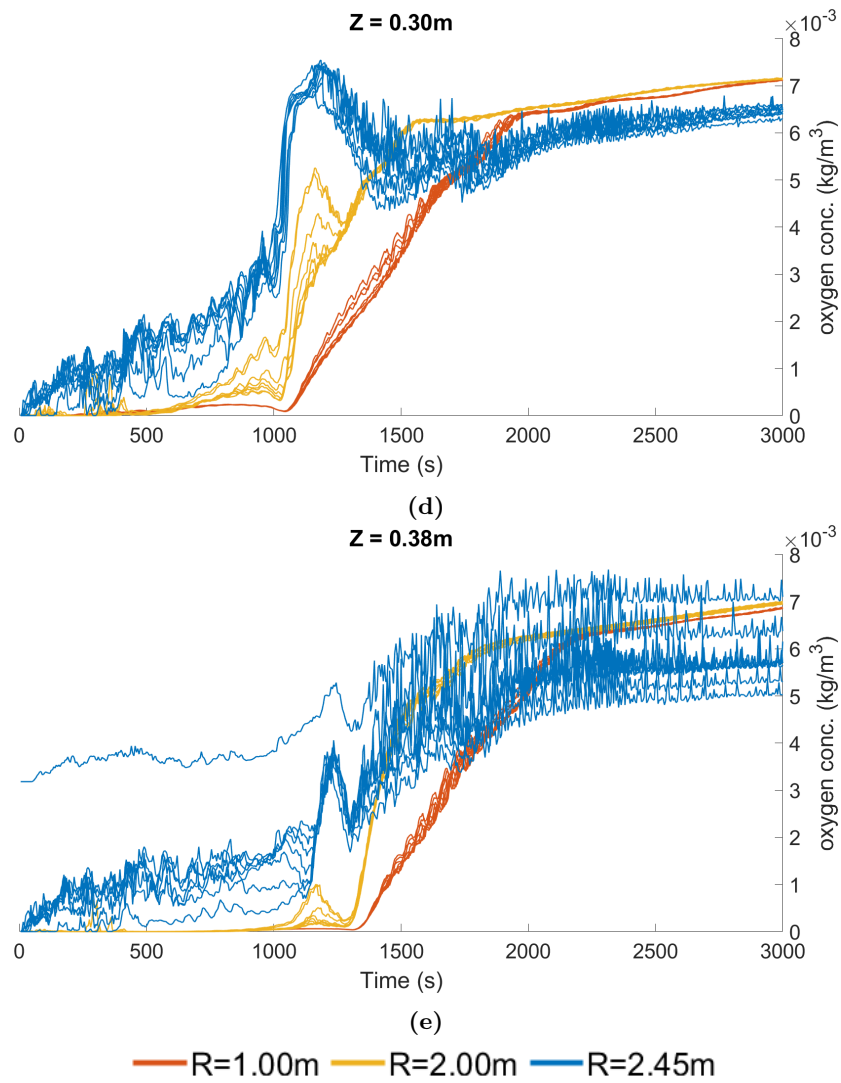
(b)

(c)
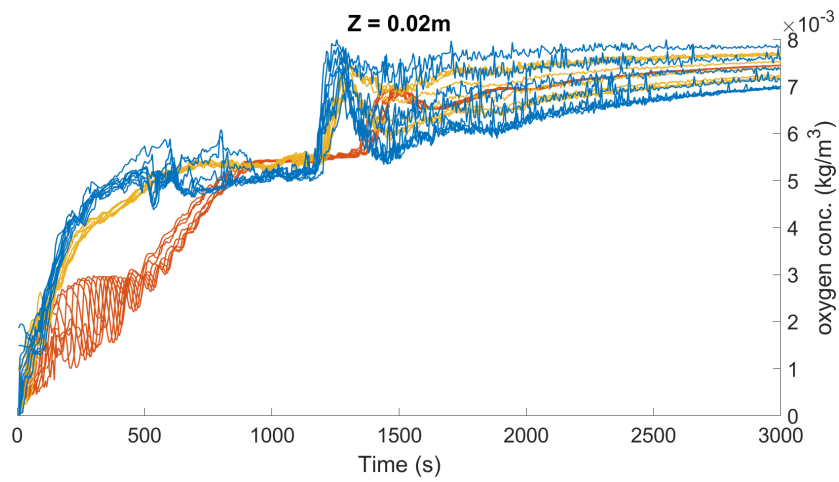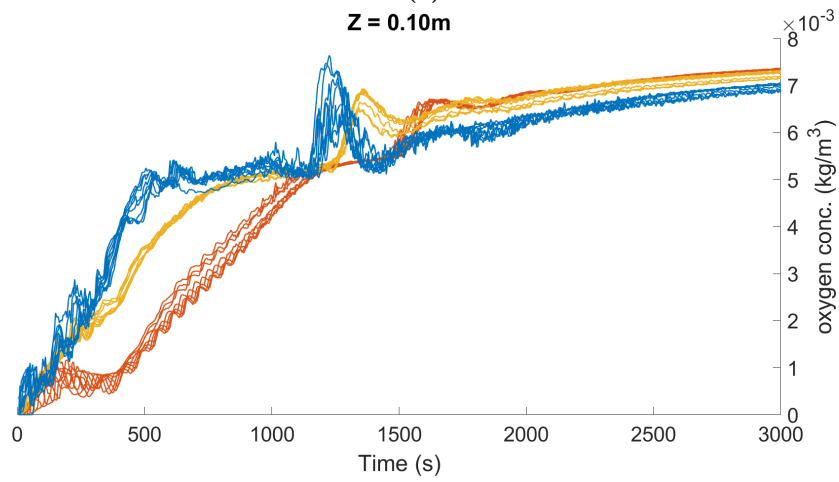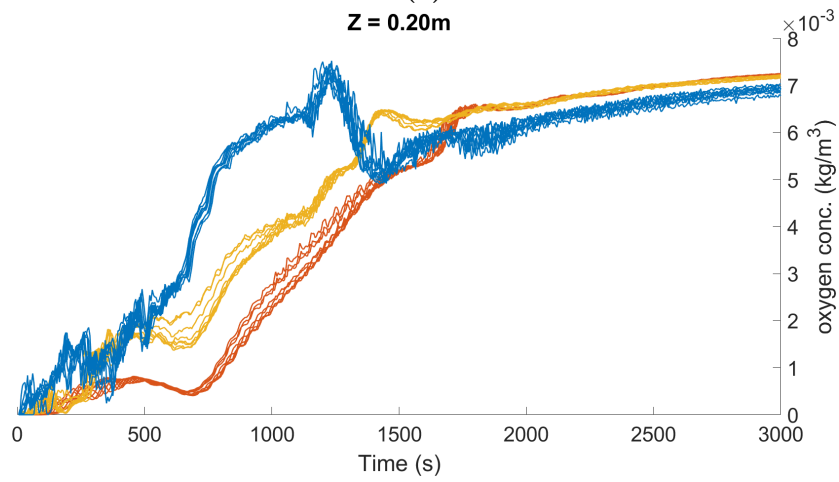
Figure 6.6: Oxygen concentration ranges for probes by Z-layer height of Case 1

Figure 6.6a shows the oxygen concentration of the lowest plane at $Z = 0.02m$. It is evident that once the fluid flow reaches steady state, there is steadily increasing dissolved oxygen content in the tank. The probes immediately register dissolved oxygen as water fills the tank. For each subsequent plot this sudden increase happens later as more time is required to fill the tank up to the different elevations.

The scalar field of the oxygen content shows fluctuations in the concentration for the probes. As the steady state velocity sets in at $t = 1500s$, the oxygen content gradually converges to the final steady state concentrations with minor fluctuation. For figure 6.6a, the range of oxygen peaks at $0.0080kg/m^3$ and has a lower limit of $0.0070kg/m^3$.

Figures 6.6b- 6.6d show many of the similar characteristics in the progression of the oxygen saturation. The difference between the bottom layer plot is the range of oxygen content is more consistent across all probes. Figures 6.6b and 6.6c share the same range of oxygen content approaching $0.0070 - 0.0075kg/m^3$ window.

Figure 6.6e shows the oxygen concentration to have large fluctuations for the probes located at radius $R = 2.45m$. There is a lone probe measurement that registers an average of $0.0040kg/m^3$ from $t = 0s$ before the flow velocity reaches a steady state. The probe's proximity to the inlet records diffused oxygen from the inlet stream which causes the same sudden increase compared to the other probes for the same layer.

The fluctuating probes are found at the outer radius of the tank where the near-wall turbulence is generated. Among the measurements there are probes that are highly consistent shown to approach $0.0070kg/m^3$ towards the end of the time steps. The surface layer has the widest range of oxygen concentration. The concentration varies in the range of $0.0050 - 0.0070kg/m^3$, which is the final range of oxygen concentration for the layer. The probe with the lowest recorded concentration levels out to a constant measurement without the steadily climbing gradient as seen in the other probes mentioned.

6.2   Case 2: Square water tank geometry (d=2.0m)

Case 2 is the first geometry where the flow velocity and oxygen concentration are distinctively different from Case 1 with the circular geometry. Case 2 geometry is the first square geometry analyzed as it is a hybrid design between circular and square tank design. Case 2 can therefore be considered a reference in the transition from circular to square geometry for the present study. Depending on the fillet radius of the tank, the impact on flow velocity and oxygen convection can be compared to different square tank geometries and their respective wall corner radius.
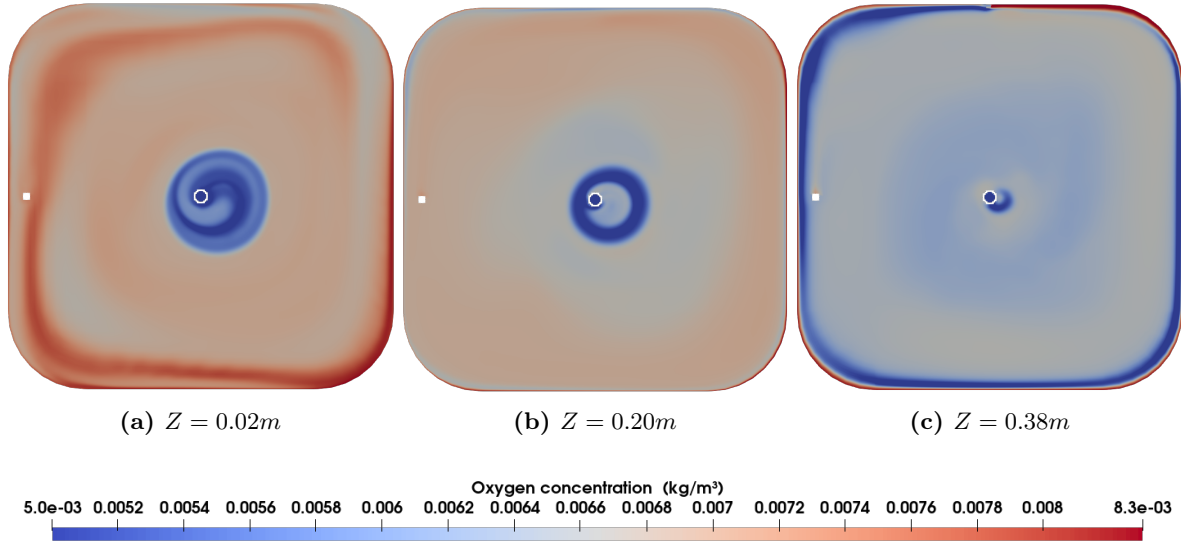

(a) $Z = 0.02m$ **(b)** $Z = 0.20m$ **(c)** $Z = 0.38m$

Oxygen concentration (kg/m³)
5.0e-03 0.0052 0.0054 0.0056 0.0058 0.006 0.0062 0.0064 0.0066 0.0068 0.007 0.0072 0.0074 0.0076 0.0078 0.008 8.3e-03

Figure 6.7: Oxygen concentration at $t = 3000s$ for different Z-layers of Case 2

(a) $Z = 0.02m$ **(b)** $Z = 0.20m$ **(c)** $Z = 0.38m$

U_rad (m/s)
0.0e+00   0.02 0.03 0.04 0.05 0.06 0.07 0.08 0.09 0.1 0.11 0.12 0.13 0.14 0.15 0.16 0.17 0.18 0.19 0.2 0.21 0.22 0.23 0.24 2.5e-01
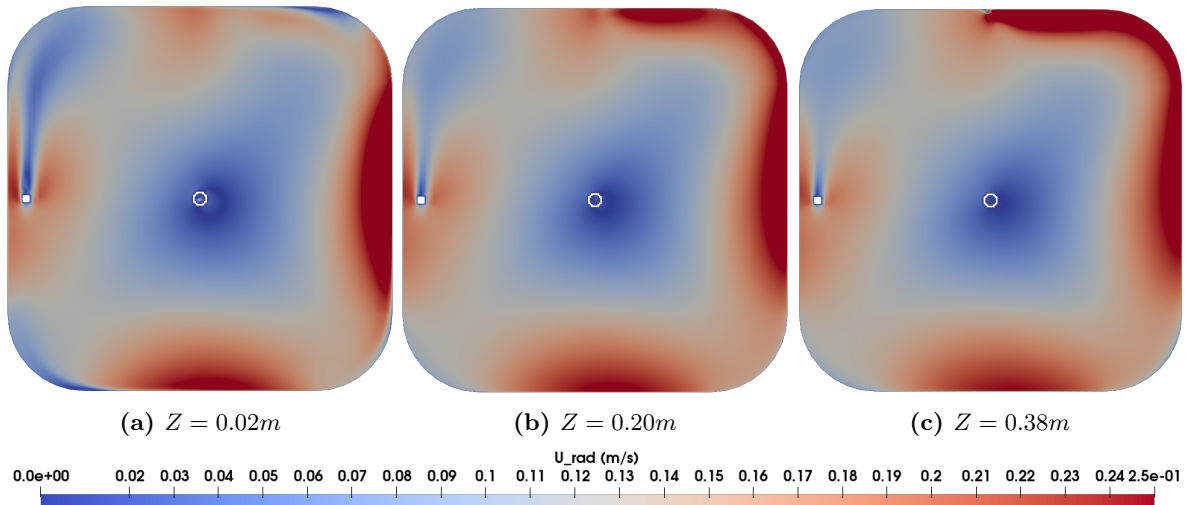
Figure 6.8: Radial velocity at $t = 3000s$ for different Z-layers of Case 2

Figure 6.7 shows contrasts to the concentration distribution from the circular water tank geometry in

figure 6.1c. The rotational symmetry of the fluid breaks due to the shape of the tank. The rate of convection of oxygen is lower due to the fluid velocity being severely reduced in respect to the tank geometry. The bottom layer in figure 6.7a shows a dense concentration coiling near the walls before the flow is directed into a spiral to dissipate the oxygen into the fluid. There is a significant drop in oxygen concentration surrounding the outlet compared to the region seen in Case 1.

The middle layer in figure 6.7b shows a more uniform concentration region with a contracting circular region with low oxygen content. Focusing on both figure 6.7a and 6.7b, it should be highlighted there is fluid flow in the vertical direction from the bottom layer up to the outlet. The trace of a spiral in the center of figure 6.7a shows an upward vortex that convects oxygen with it. It explains why the low-concentration region in figure 6.7b is hollow.

In figure 6.7c there is lower oxygen content in the top surface layer compared to Case 1. The inlet injects oxygenated water that quickly dissipates into the rest of the tank volume and lower depths.

Figure 6.8 shows that the radial velocity is predominantly higher at the straight wall sections of the tank. The main reason for the phenomenon is due to the diffusion of the radial velocity being impacted by the shape of the tank. The radial velocity is nearly uniform in circular motion, however the fluid in any square tank is going in a semi-circular flow. The velocity in the cross-sections are significantly lower than those of Case 2. The legend for the square tank cases are decreased from $0 - 0.50m/s$ to $0 - 0.25m/s$, which further highlights the decrease in radial velocity in the plane.

Figure 6.8a shows the radial velocity to be dominant at the eastern straight wall section, with a peak region at the x-axis perpendicular to the outlet. The fluid shows a parabolic region where there is increase in radial velocity followed by a decline, which is a consequence from equation 23 for radial velocity calculation. The parabolic shape of the radial velocity is due to the shape of the tank affecting the calculated radial velocity. Any fluid particle (P) in the tank has a distance between it and the overflow outlet in the center of the tank. The distance between P and the outlet is a radius in terms of polar coordinates. As the particle flows linearly along the wall, there is changing radial velocity dr/dt.
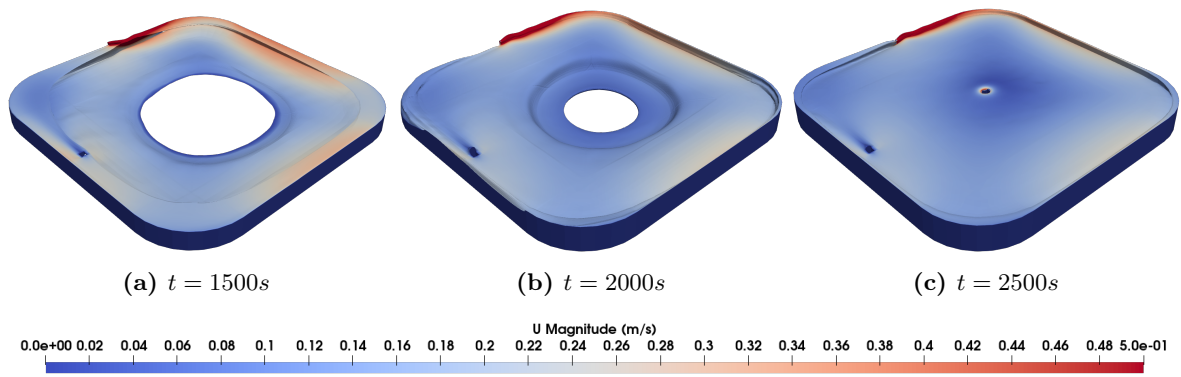
(a) $t = 1500s$ **(b)** $t = 2000s$ **(c)** $t = 2500s$

Figure 6.9: Oxygen distribution above $0.0050kg/m^3$ over time intervals t of Case 2

Figure 6.9 shows the oxygen concentration of the tank over time intervals. It can be seen that the oxygen distributes from the wall sections of the tank at $t = 1500s$ before the transport reaching the center of the tank. At the end interval the tank approaches equilibrium near the outlet. The void in the center of the figure is the dome-shaped low-concentration region.
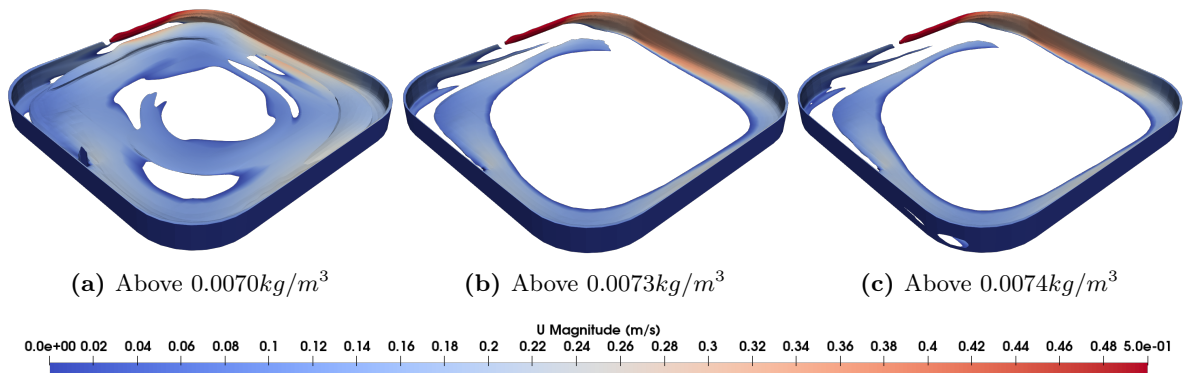

(a) Above $0.0070kg/m^3$ **(b)** Above $0.0073kg/m^3$ **(c)** Above $0.0074kg/m^3$

Figure 6.10: Oxygen distribution isosurfaces at $t = 3000s$ for different thresholds of Case 2

Figure 6.10 shows oxygen concentration having a lower distribution in the tank, particularly towards the center of the water tank. Most of the dissolved oxygen is located at the walls of the tank, due to reduced velocity at the boundary layer keeping oxygen from being transported in the free stream of the water. As the threshold is increased in figure 6.10a to 6.10b there is less oxygen in the center volume that can keep high saturation. Figure 6.10b shows a limit being reached where the stream of oxygen content diffuses into the fluid. The circular geometry as shown in figure 6.4c has a distribution that reaches closer to the outlet near the bottom plane of the tank.

6.2.1   Radial velocity

The general observations of radial velocities seen in figure 6.11 compared to Case 1 results are that the overall velocities are lower, with broader range. At $R = 1.00m$, the velocity is now decreased from

$0.12 - 0.16 m/s$ range to $0.06 - 0.11 m/s$. The reduced velocity means the water has lower recirculation in the domain. In figure 6.11, the range difference is distinguishable, since the velocities recorded is in the range of $0.10 - 0.37 m/s$ as opposed to the circular geometry that has a range of $0.25 - 0 - 50 m/s$.
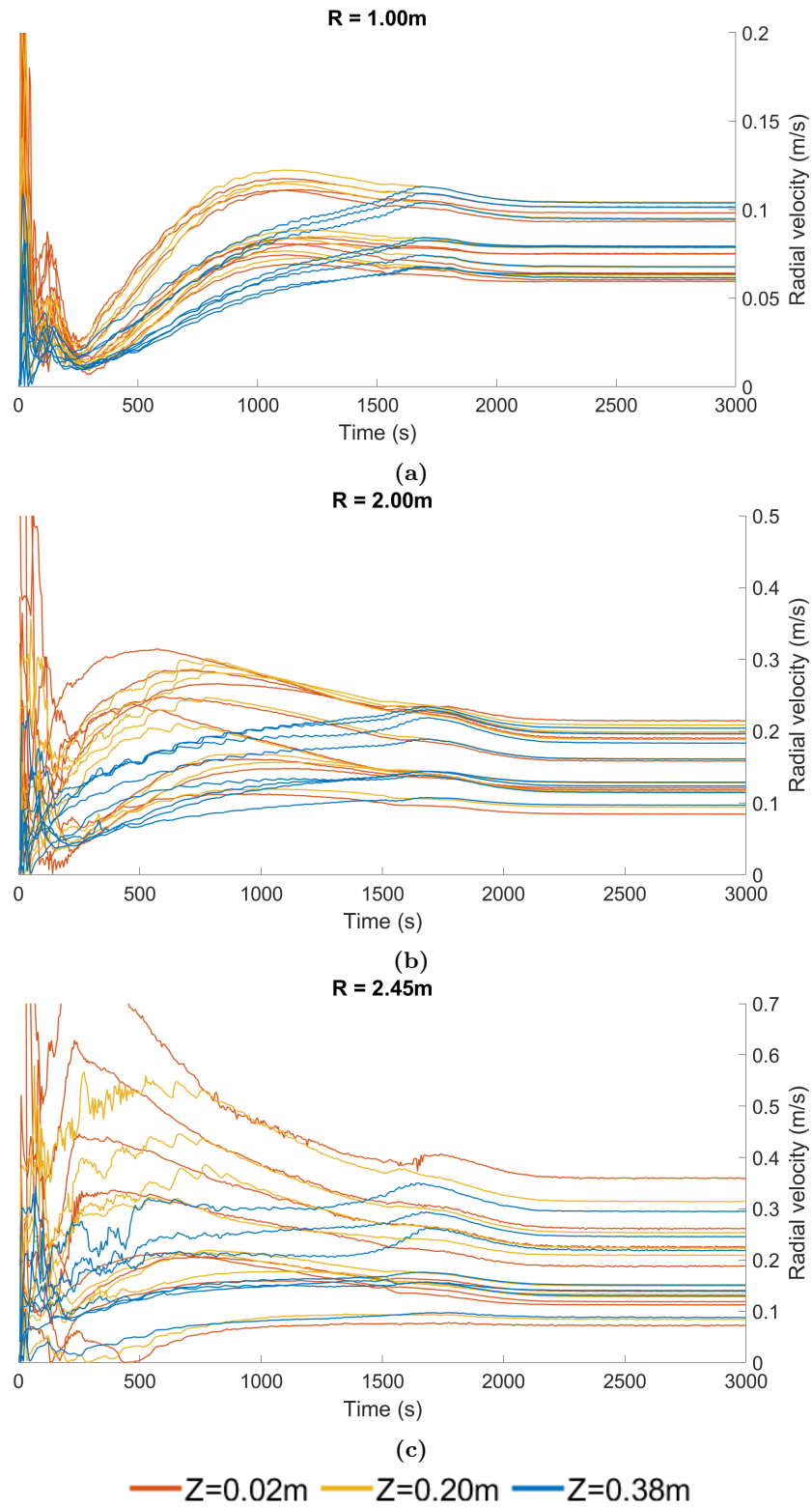
**Figure 6.11:** Radial velocity results at probes by radii for Case 2

Furthermore, the velocity recordings seem to separate into distinct ranges, depending on their position in the tank. Figure 6.8 and figure 6.11 can be compared to show the split in velocities. The plotted velocities at $R = 2.00m$ show four grouped ranges of velocities emerging in the steady state flow. The four groups show that the radial velocity is dependent on the flow field from the inlet in the clockwise direction. The velocity decreases for each quadrant of the tank the flow passes.
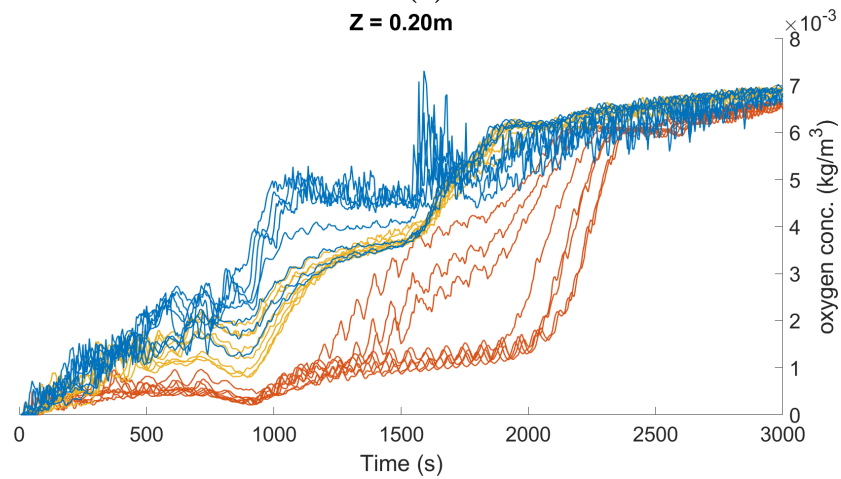
6.2.2   Oxygen concentration

Figure 6.12 shows the oxygen concentrations to be converging towards a distinct range for each layer height. The measurements are fluctuating to a larger extent than seen in figure 6.6 for Case 1. The concentrations are steadily climbing at $t = 3000s$ which means further simulation could be conducted to get a further steady state. The concentration range stays consistent for the first two layers; $Z = 0.02m$ and $Z = 0.10m$. The maximum concentration reached by each plane for the duration of the simulation decreases with higher layer height.
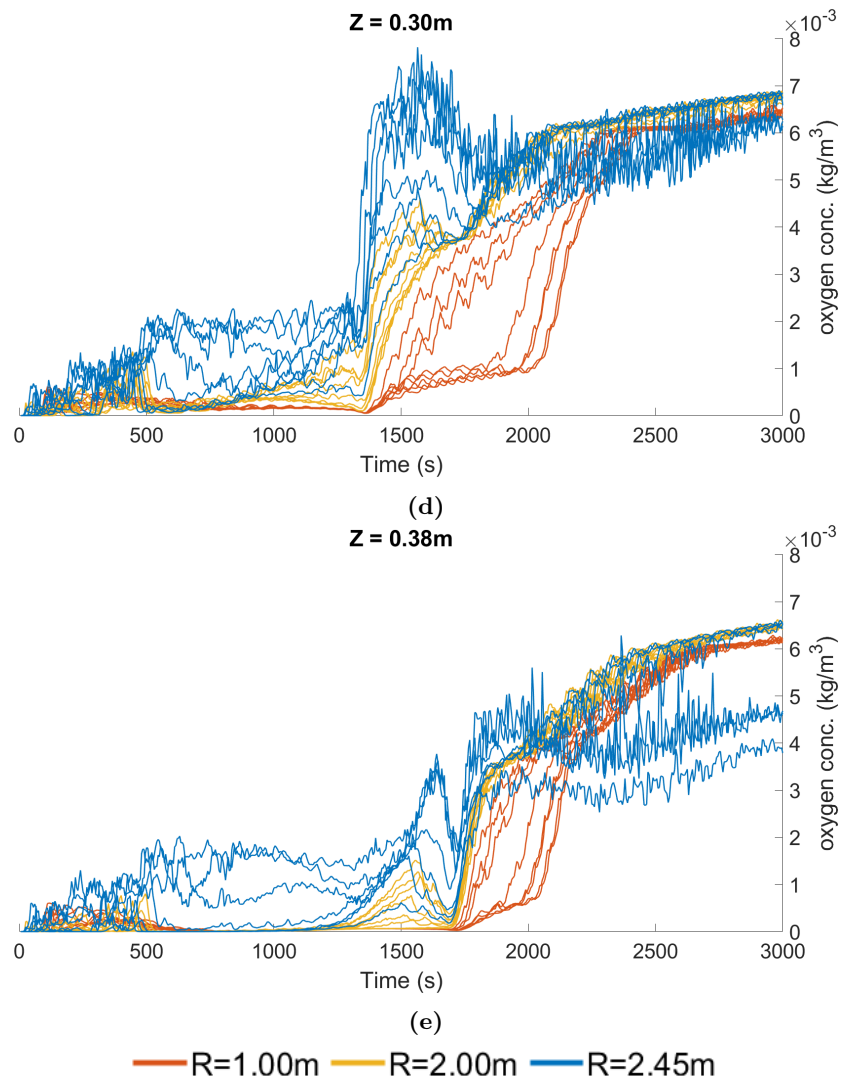
(a)

(b)

(c)
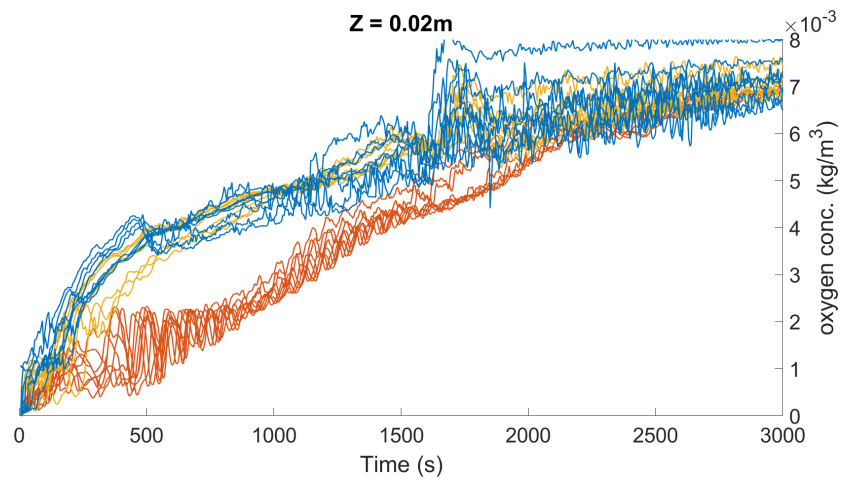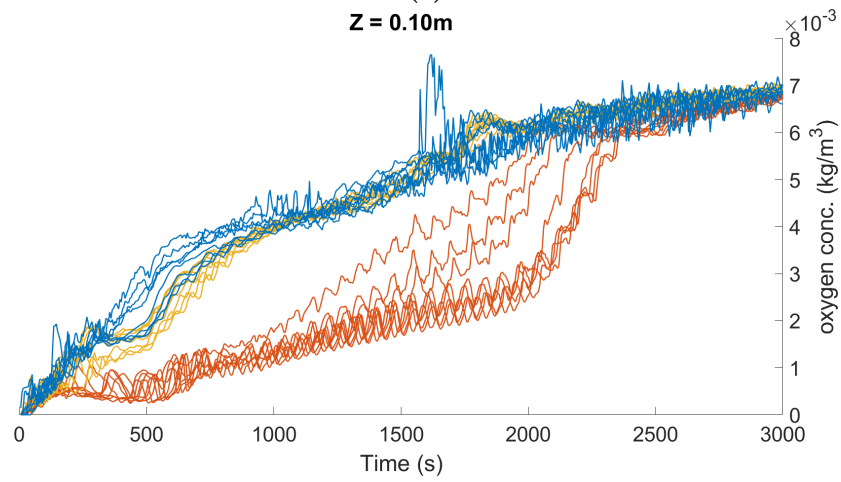
Figure 6.12: Oxygen concentration ranges for probes by Z-layer height of Case 2

Figure 6.12a is evidently fluctuating and reaches a range in concentration of $0.0065 - 0.0075kg/m^3$. Figures 6.12b and 6.12c share similar characteristics in their oxygen content progression. The concentrations steadily rise with a consistent range of oxygen concentration. The main difference between the two plots is the probes climbing towards higher measured oxygen content happens later for figure 6.12c as the water fills the tank.

Figures 6.12d and 6.12e show the concentrations for the top layers. In these plots it is possible to differentiate between the fluctuating and steady concentrations. The two probes that drop below $0.005kg/m^3$ are positioned at $R = 2.45m$ and $\theta = 0°$. The wall section near the probe location does not capture diffused oxygen because the oxygen is convected to the free stream. The oxygen is convected once the inlet stream travels to the corner wall in the northeast section of the tank.

An important observation for all the plots in figure 6.12 is the oxygen concentration for probes located at $R = 1.00m$. The probes show there is difficulty in saturating the center of the tank as shown in figure 6.1a. The reduced convection of oxygen due to low flow velocity means there is less oxygen distribution towards the center of the tank.

6.3   Case 3: Square water tank geometry (d=1.5m)

Figure 6.13 shows the dissolved oxygen distribution of Case 3. The presented scalar field graphics show nearly identical patterns in the convection of oxygen from Case 2. A minor difference between the presented graphics are the low concentration areas of each layer are slightly less saturated. In figure 6.13c, the concentration is slightly lower in the flow around the outlet. A small ring at the top layer is visible. The change in fillet radius shows a larger void in oxygen concentration in the bottom layer of the tank.

(a) $Z = 0.02m$ (b) $Z = 0.20m$ (c) $Z = 0.38m$

Oxygen concentration (kg/m³)
5.0e-03 0.0052 0.0054 0.0056 0.0058 0.006 0.0062 0.0064 0.0066 0.0068 0.007 0.0072 0.0074 0.0076 0.0078 0.008 8.3e-03
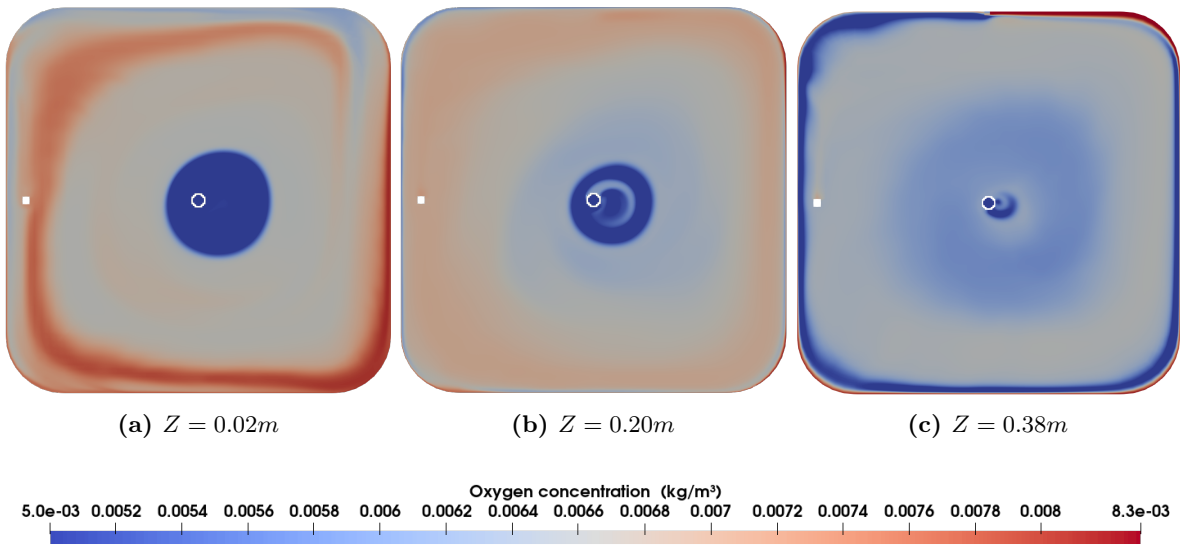
Figure 6.13: Oxygen concentration at $t = 3000s$ for different Z-layers of Case 3

(a) $Z = 0.02m$ **(b)** $Z = 0.20m$ **(c)** $Z = 0.38m$

U_rad (m/s)

0.0e+00   0.02 0.03 0.04 0.05 0.06 0.07 0.08 0.09 0.1 0.11 0.12 0.13 0.14 0.15 0.16 0.17 0.18 0.19 0.2 0.21 0.22 0.23 0.24 2.5e-01
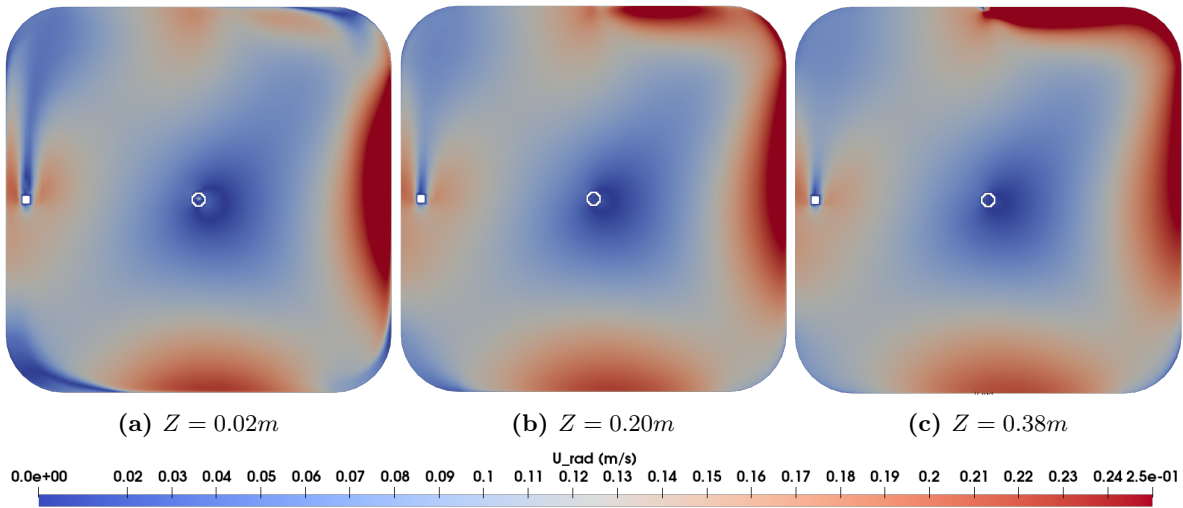
Figure 6.14: Radial velocity at $t = 3000s$ for different Z-layers of Case 3

Figure 6.14 show the largest magnitude of radial velocity occurs at the eastern wall, as well near the jet of the inlet at the top layer of $Z = 0.38m$. In similar observation to Case 2, the radial velocity diminishes for each wall encountered by the flow as the water travels in the clockwise direction.

An important observation for the slices show the radial velocity is highest at the eastern wall, however the oxygen concentration is not saturated by the oxygen convecting from the eastern wall. Figure 6.13a shows the low concentration region that skews towards the eastern wall. The higher tangential velocity of the water at the east wall means the water will travel past the outlet in short time. At the western wall, the fluid travels slower, which means despite low radial velocity, the water has a longer time period to travel radially towards the outlet. This phenomenon results in the skewed low-concentration region being saturated from the western quadrant towards the outlet.
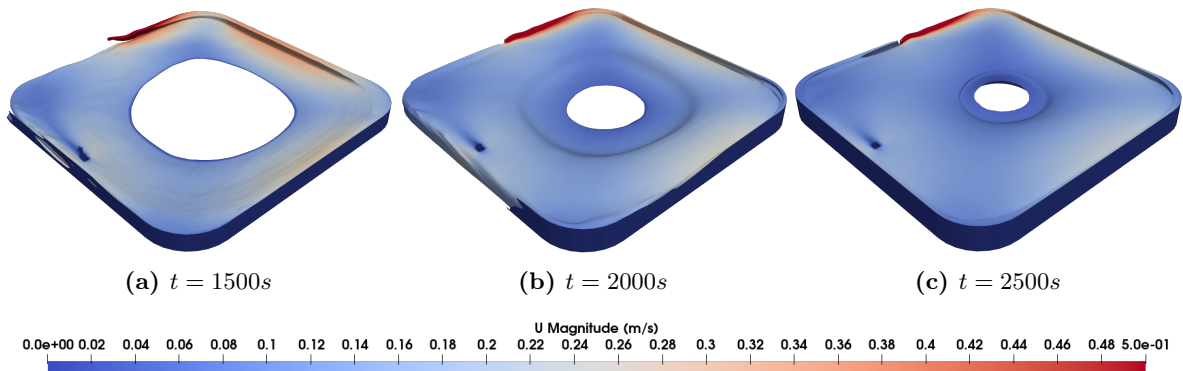

(a) $t = 1500s$ **(b)** $t = 2000s$ **(c)** $t = 2500s$

U Magnitude (m/s)

0.0e+00 0.02   0.04   0.06   0.08   0.1   0.12   0.14   0.16   0.18   0.2   0.22   0.24   0.26   0.28   0.3   0.32   0.34   0.36   0.38   0.4   0.42   0.44   0.46   0.48 5.0e-01

Figure 6.15: Oxygen distribution above $0.0050kg/m^3$ over time intervals t of Case 3

Figure 6.15 shows the distribution of oxygen concentration above $0.0050kg/m^3$ as the tank fills up over time. The progression in oxygen convection shows the walls and bottom part of the domain saturating at first before the oxygen diffuses towards the center of the tank. The low concentration regions as

seen in figure 6.13 are below the threshold for the isosurface. Therefore observing the isosurface from below reveals a half-spherical volume where the isosurface is empty. Figure 6.15c shows a hole in the middle of the surface, which is the low concentration volume as shown in 6.13.
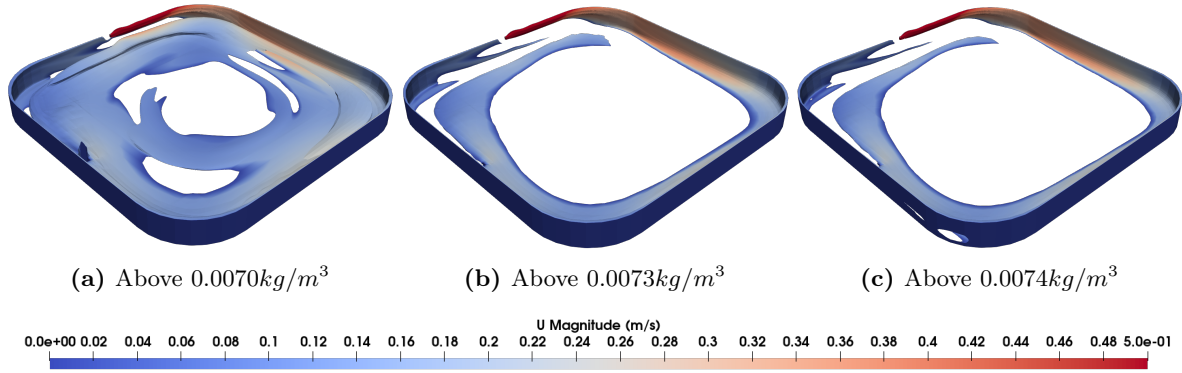

(a) Above $0.0070 kg/m^3$ **(b)** Above $0.0073 kg/m^3$ **(c)** Above $0.0074 kg/m^3$

Figure 6.16: Oxygen distribution isosurfaces at $t = 3000s$ for different thresholds of Case 3

Figure 6.16 shows the same threshold limits as used in figure 6.10 for the square-shaped tanks. The $0.0070 kg/m^3$ concentration threshold for figure 6.16a shows a prominent hole in the center where the low-concentration dome-shaped region is even larger compared to the Case 2 results. Figure 6.16b shows the oxygen concentration slightly lowered in volume, but is still prominent in the tank near the bottom and the walls. Figure 6.16c shows similarities compared to Case 2, except the flow completes one revolution around in the tank before dissipating to lower concentration regions near the center of the tank.

6.3.1   Radial velocity

The radial velocities measured for Case 3 in figure 6.17 show the same trends in velocity as for Case 2 in figure 6.11. The difference for the velocities is the magnitude of the recorded measurements between Case 2 and Case 3. The difference can be described as incremental by comparison to the velocities recorded in Case 2.
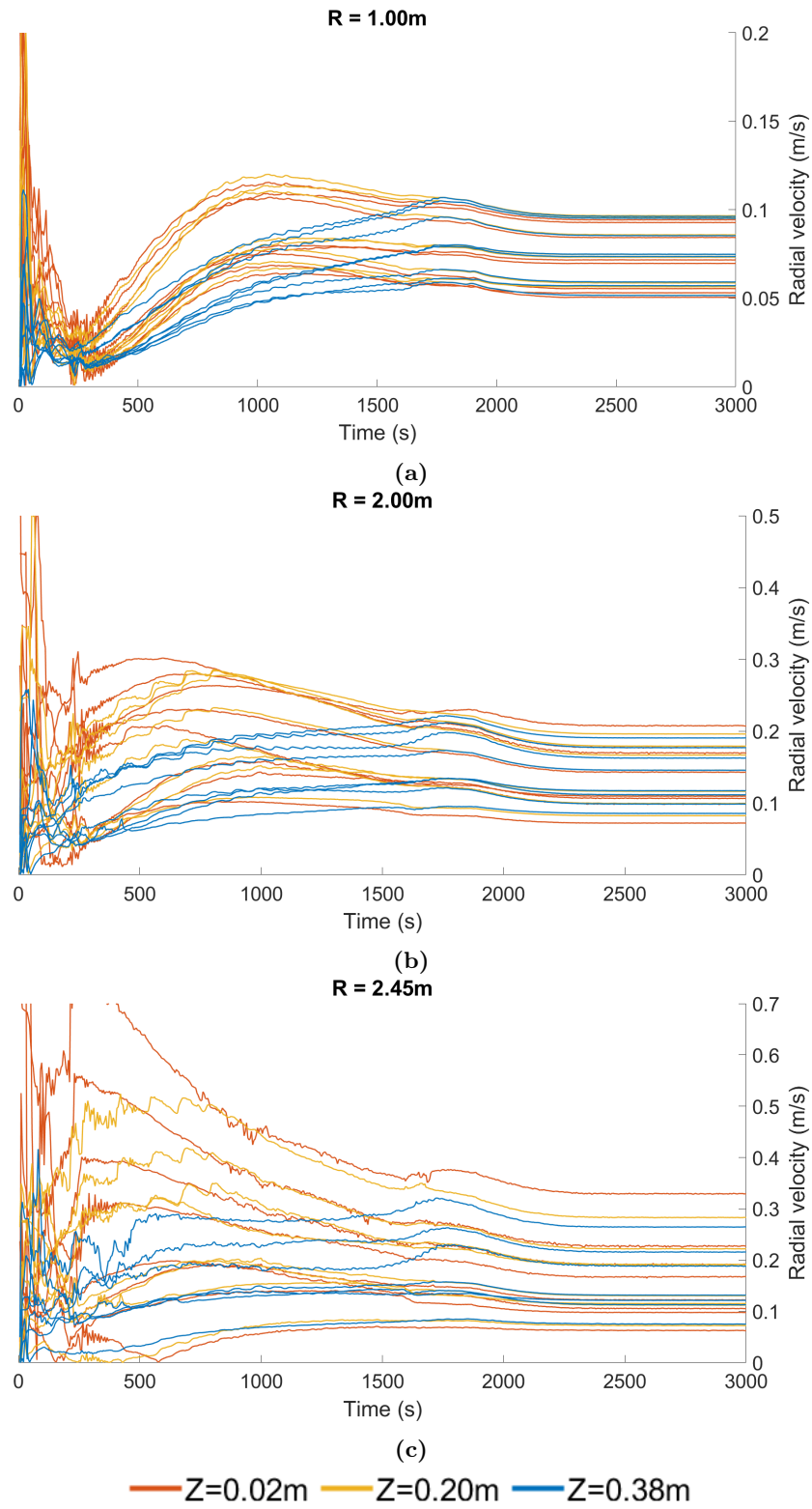
(a)

(b)

(c)

**Figure 6.17:** Radial velocity results at probes by radii for Case 3

Figure 6.17a show the velocities at $R = 1.00m$ exist in the range of $0.05-0.10m/s$. The difference from Case 2 for the new velocity range is nearly identical and show that the geometry effect on velocity is low for the inner radius of the tank. Figure 6.17b at $R = 2.00m$ has a velocity range of $0.07-0.21m/s$. The range is also slightly reduced by the geometry, however the extent of impact by the geometries for the step between Case 2 and Case 3 is too limited to draw definitive conclusions. In the comparison section, the relationship between the velocities and tank geometry are directly compared. Figure 6.17c show the velocities at $R = 2.45m$ reach equilibrium with a range of $0.06 - 0.33m/s$. The result is as expected and show the same tendency and velocity distribution. The only apparent difference is the decrease in radial velocity.
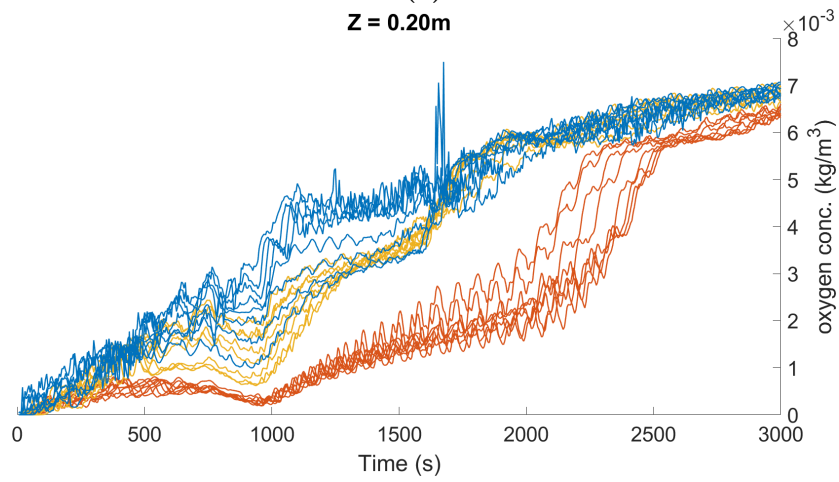
6.3.2   Oxygen concentration

The dissolved oxygen concentrations shown in figure 6.18 show the concentrations have smaller fluctuations than those in Case 2. An important fact regarding the plots that needs to be addressed is that there is still slight linear increasing in the oxygen concentration at the end of the simulation run. The concentrations are expected to climb further in a logarithmic trend as seen with previous cases. For the results and discussion section, the final measurements are used for comparison.
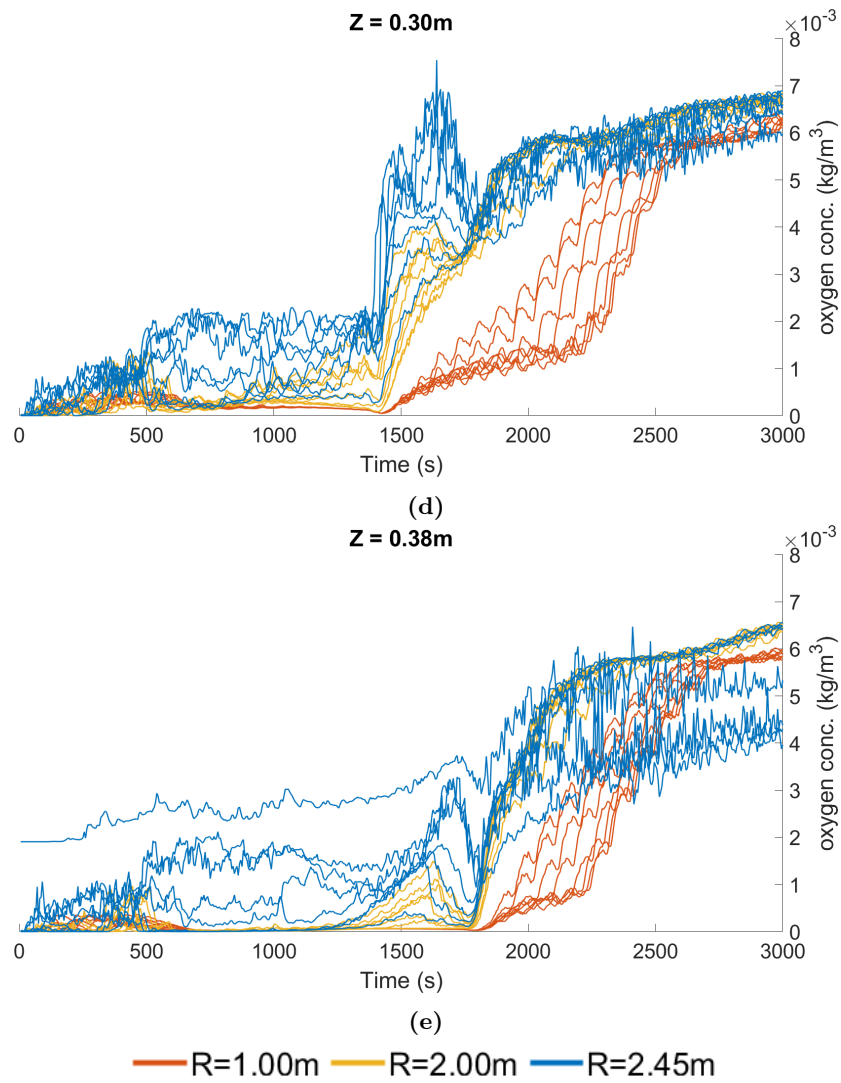
(a)

(b)

(c)

(d)

(e)
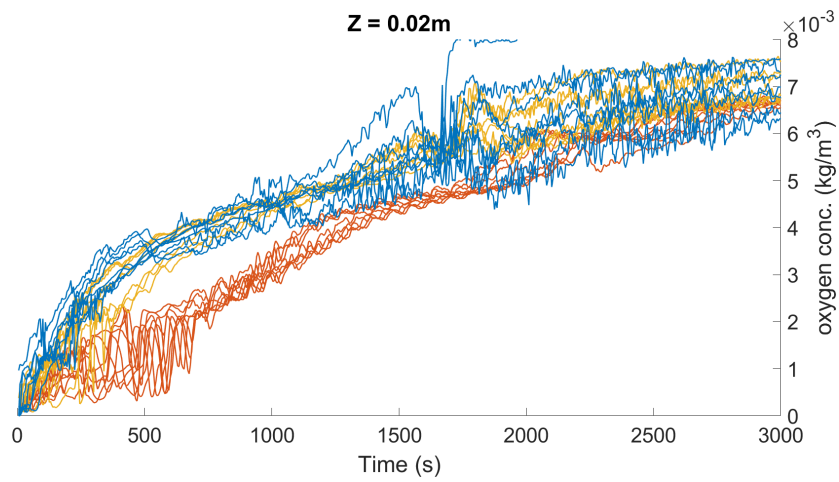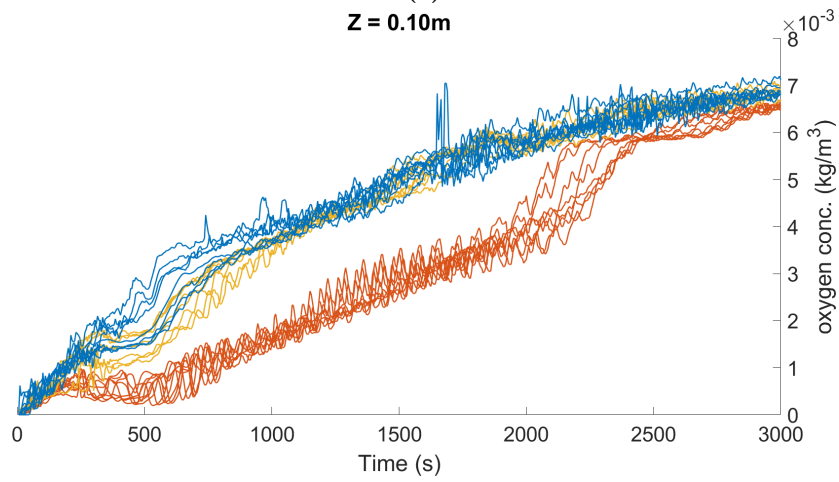
Figure 6.18: Oxygen concentration ranges for probes by Z-layer height of Case 3

Figure 6.18a show the bottom layer at $Z = 0.02m$ which has probes measuring several points with low oxygen content. Considering the bottom layer has the benefit of saturating with oxygen early on, the measurements show a lack of oxygen in the bottom plane at $t = 3000s$. The range of oxygen is found at $0.0061 - 0.0075kg/m^3$, which is larger than previous discussed cases.

Figures 6.18b-6.18d show the probe measurements are consistent across the layer, with minor fluctuation and steady range. The measurements fall below $0.0070kg/m^3$ with increasing layer height, which is also evident in the clips shown in figure 6.16. Figure 6.18e has a significant drop in saturation which peaks at $0.0065kg/m^3$. The concentration towards the tank center at $R = 1.00m$ increases steadily behind the other probes before climbing at a higher rate towards the end of the simulation. The dissolved oxygen content at $R = 1.00m$ is higher than some of the probes at $R = 2.45m$ which shows that the surface region has low convection of dissolved oxygen at the walls.

6.4   Case 4: Square water tank geometry (d=1.0m)

Figure 6.19 shows the oxygen transport in Case 4 with the sharpest fillet radius. In this case it is clear there is less uniform distribution of oxygen in the bottom layer. The western and northern walls of the slices show a lack of diffused oxygen at the walls. The oxygen diffuses into the domain in a spiral which is evident from the lines formed in the figure showing a region with higher concentration. Figure 6.20b shows the concentration to be most uniform of all three presented layers, which also contain the same characteristics seen in the other square tank geometries for the layer. There is a trace of low oxygen content in the southwest region of the layer, however it is small. Figure 6.19c shows the oxygen content to stay in line with the wall before dissipating into the domain. The velocity of the fluid slows down when reaching the first corner, which means the oxygen slowly dissipates in the tank.
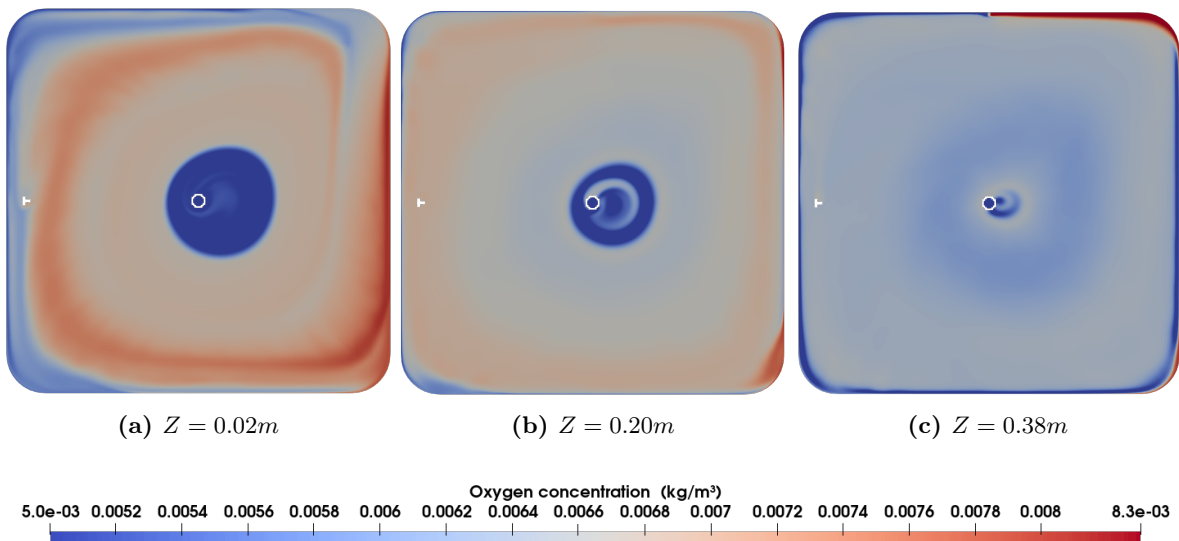

(a) $Z = 0.02m$ **(b)** $Z = 0.20m$ **(c)** $Z = 0.38m$

Figure 6.19: Oxygen concentration at $t = 3000s$ for different Z-layers of Case 4

(a) $Z = 0.02m$ **(b)** $Z = 0.20m$ **(c)** $Z = 0.38m$

U_rad (m/s)

0.0e+00   0.02 0.03 0.04 0.05 0.06 0.07 0.08 0.09 0.1 0.11 0.12 0.13 0.14 0.15 0.16 0.17 0.18 0.19 0.2 0.21 0.22 0.23 0.24 2.5e-01
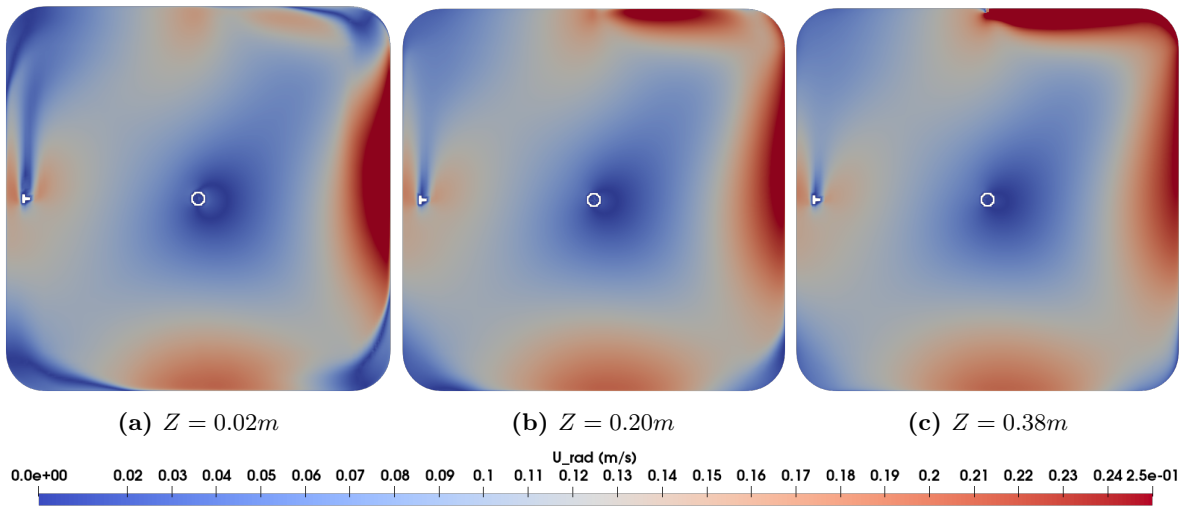
Figure 6.20: Radial velocity at $t = 3000s$ for different Z-layers of Case 4

Figure 6.20 shows the radial velocities for Case 4. It shows a larger variation in radial velocity for each wall in the tank. The velocity is highest at the eastern wall and decreases with each succeeding corner. There are regions visible in the corners of figure 6.20a where the radial velocity is near still, which is due to the fluid moving away from the outlet. The interesting feature about the low velocity regions is the flow is due to the viscous effects by the wall. The fluid then carries more radial velocity due to the pressure effect on the fluid.
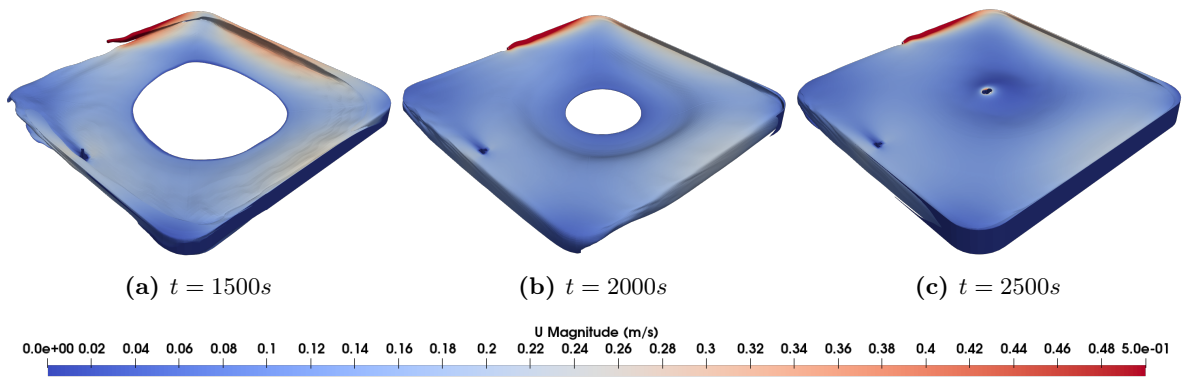

(a) $t = 1500s$ **(b)** $t = 2000s$ **(c)** $t = 2500s$

U Magnitude (m/s)

0.0e+00 0.02   0.04   0.06   0.08   0.1   0.12 0.14 0.16 0.18 0.2 0.22 0.24 0.26 0.28 0.3 0.32 0.34 0.36 0.38 0.4 0.42 0.44 0.46 0.48 5.0e-01

Figure 6.21: Oxygen distribution above $0.0050kg/m^3$ over time intervals t of Case 4

Figure 6.21 shows the distribution of oxygen concentration above $0.0050kg/m^3$ as the tank fills up over time. The progression of the oxygen saturation is similar to Case 3. The minor difference is the distribution of oxygen at the walls which is not visible in the western straight wall section at $t = 2500s$.
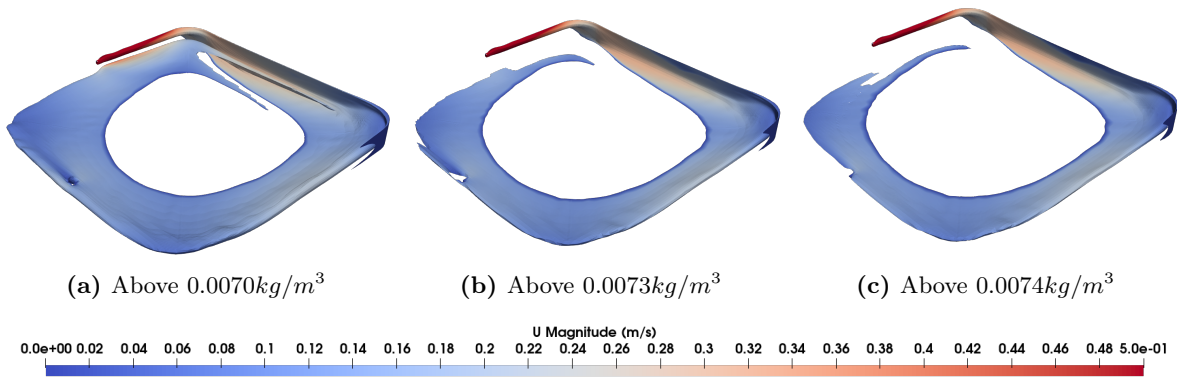
(a) Above 0.0070kg/m^3 **(b)** Above 0.0073kg/m^3 **(c)** Above 0.0074kg/m^3

Figure 6.22: Oxygen distribution isosurfaces at $t = 3000s$ for different thresholds of Case 4

Figure 6.22 shows the diffused oxygen content to be difficult to transport in the square tank geometry with sharpest fillet corners. It is visible that the oxygen content above $0.0070kg/m^3$ is mostly distributed in the bottom plane of the tank, with oxygen at the eastern walls. It is clear there is a lack of oxygen distributed to the center of the tank since content above $0.0074kg/m^3$ can make one full cycle in the tank before the content drops below the isosurface threshold.

6.4.1   Radial velocity

The radial velocities in figure 6.23 show the same trend that is visible from the previous cases for square geometry. There is a slight reduction in velocity, with the probe measurements staying consistent in their velocity distribution. The highest radial velocity is achieved at the eastern wall, which from figure 6.23c is $0.30m/s$.
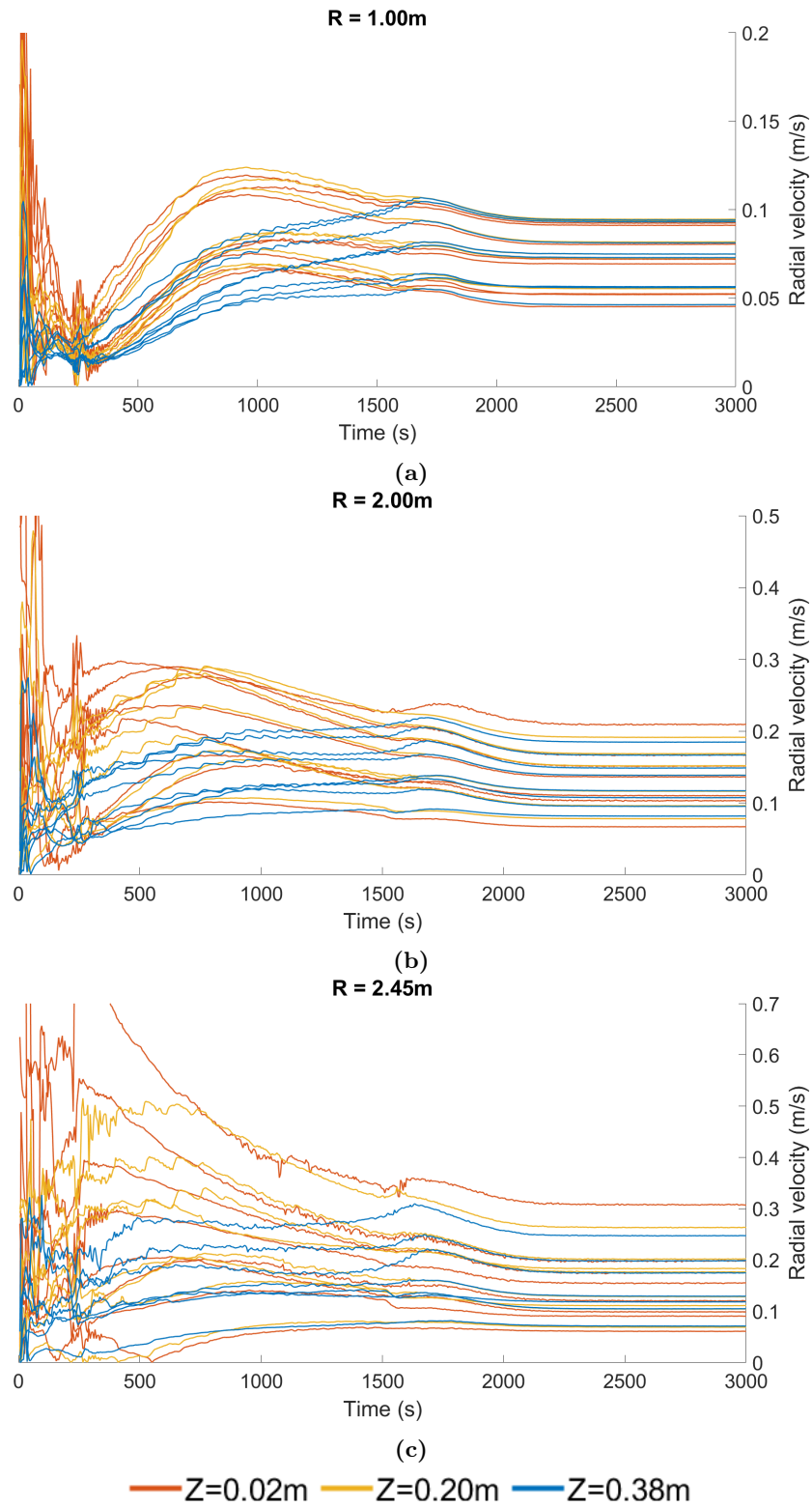
**Figure 6.23:** Radial velocity results at probes by radii for Case 4

Figure 6.23a shows that the probes at $R = 1.00m$ have differing radial velocities, which means the fraction of water volume removed from the system at the outlet favors a specific area of the tank. It means for some probes which record a velocity of $0.10m/s$, the recirculation from the particular direction is twice as high as the direction where the velocity is $0.05m/s$. The disparity in radial velocity compared to the range measured for circular geometry is an apparent disadvantage with square water tank geometries.

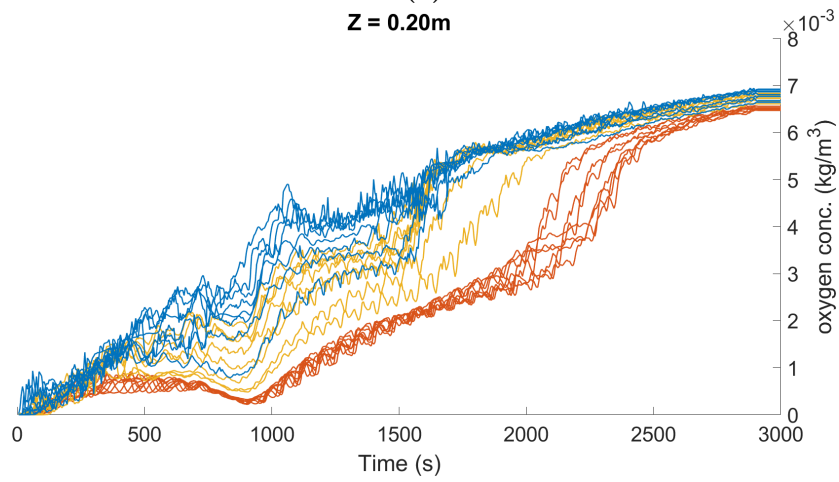### 6.4.2   Oxygen concentration

Figure 6.24 shows the concentrations. The plots are consistent with low fluctuations in oxygen concentration. Figure 6.24a shows most of the probes range in oxygen concentration in the interval $0.0060 - 0.0075kg/m^3$. The lowest reading is achieved at P3, where the oxygen concentration is influenced by the concentration void at the outlet seen in figure 6.19a. The highest recorded oxygen content is located at P19 which is located at $R = 2.45m$ and $\theta = 90°$.
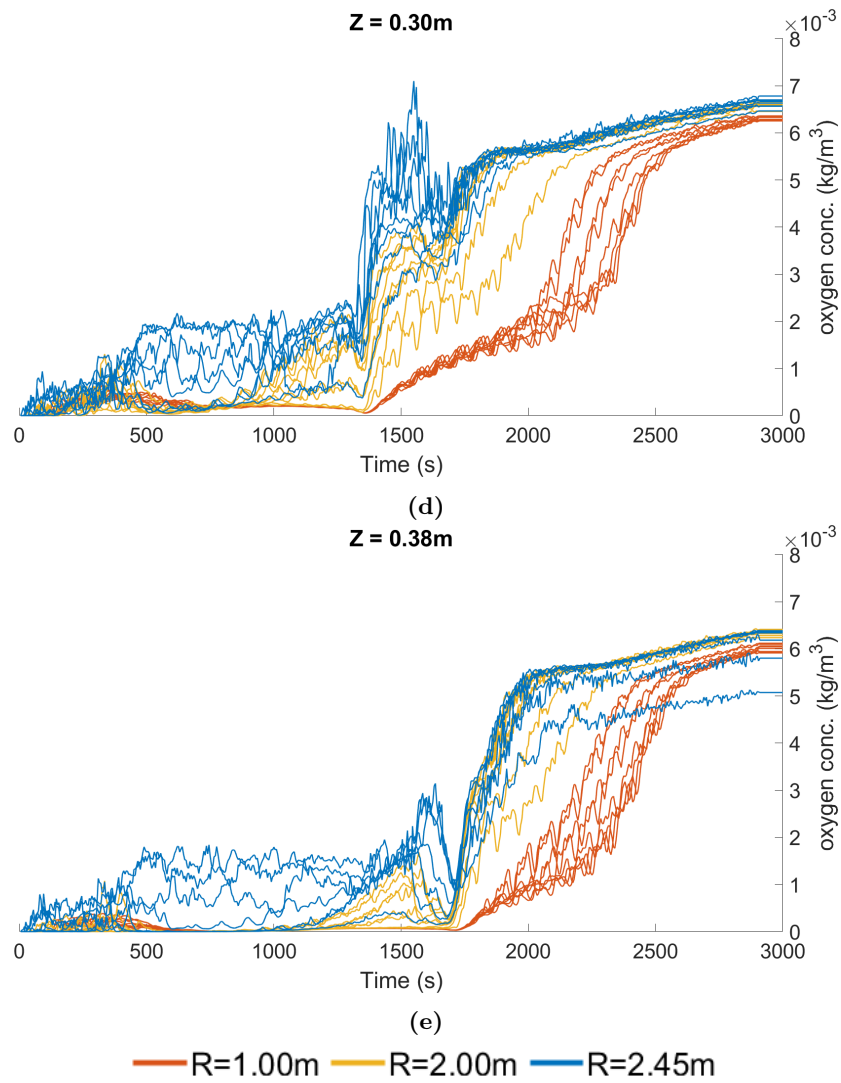
(a)

(b)

(c)

(d)

(e)
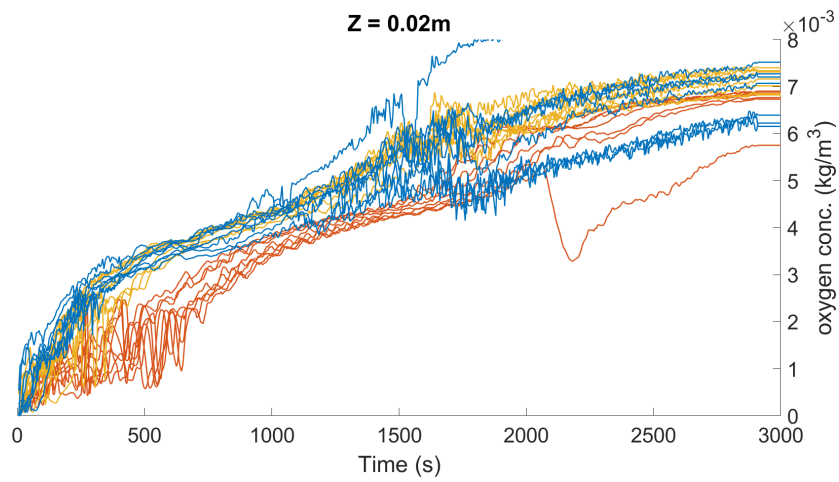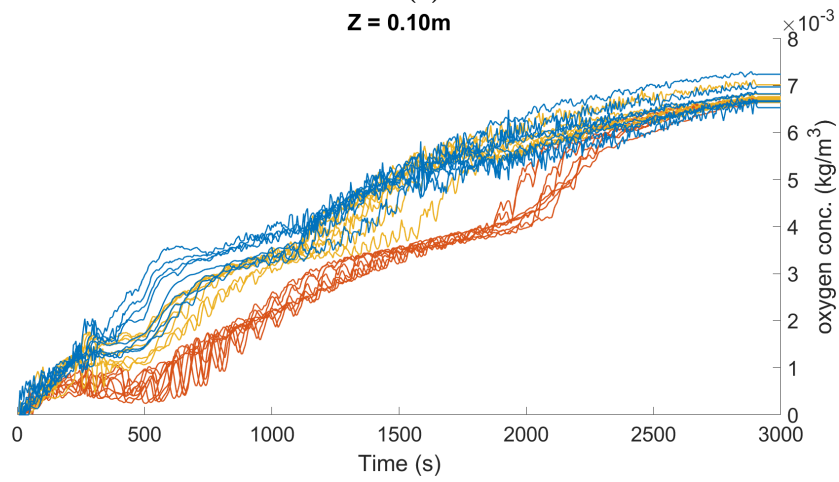
Figure 6.24: Oxygen concentration ranges for probes by Z-layer height of Case 4

Figure 6.24b shows a range of $0.0065 - 0.0073 kg/m^3$ in oxygen content at $Z = 0.10m$. The variation in range is consistent for the layers, but are overall diminished with increasing layer height. This observation is consistent with the isosurfaces shown in figure 6.22. The oxygen concentration is not evident above $Z = 0.10m$ in the isosurfaces. Figure 6.24e is consistent with the rest of the square tank geometries which has a consistent oxygen content range of $0.0058 - 0.0065 kg/m^3$

6.5   Comparison

In this section, the four cases are compared to show the difference in oxygen saturation and final radial velocities of the tank geometries. A few probe locations are selected to show the flow field dependence on tank geometry. The points selected for comparison are the same as used in the convergence study. The probes show the final oxygen concentrations and radial velocities at P23, P15 and P7.
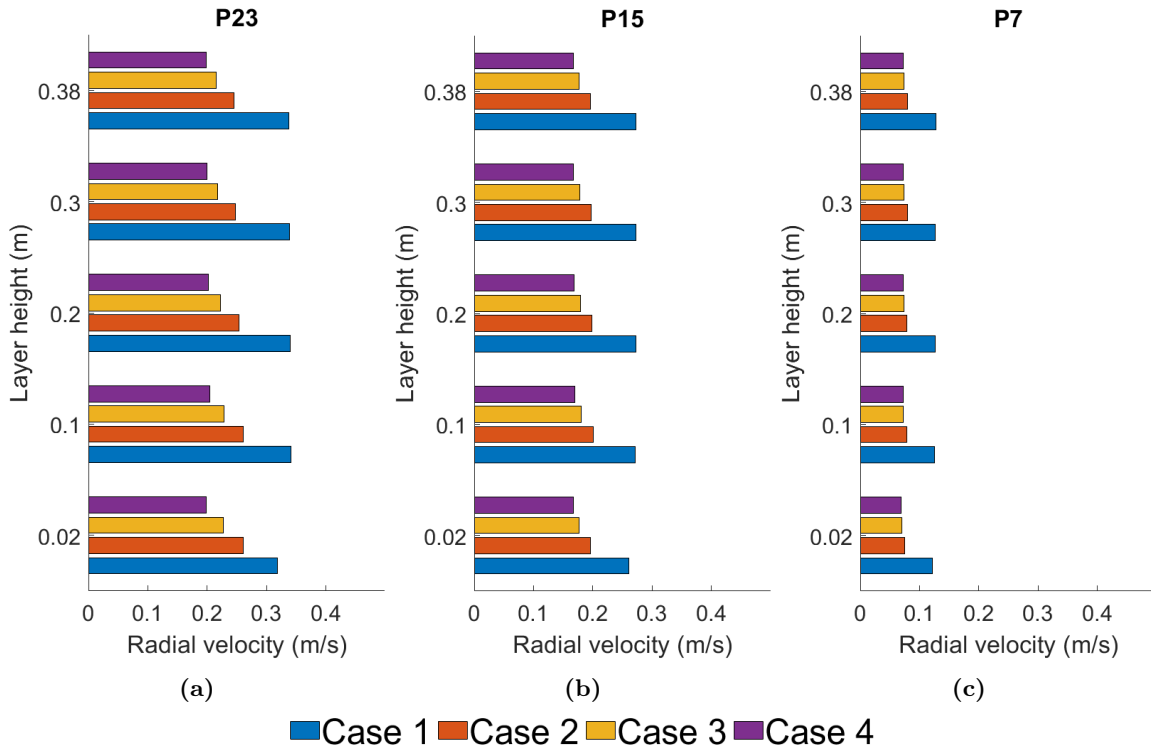

Figure 6.25: Comparison between radial velocity at probe locations across cases at $t = 3000s$

Figure 6.25 shows the steady state radial velocity at a selection of probes for different cases. The bar charts show the y-axis to be the velocity at each layer height, with the x-axis indicating the measured radial velocity. The probes are selected due to their positioning, which gives relevant data for the developed fluid flow in the domain. In the figures, it is apparent the free stream velocity from the tank bottom is linear, with a small decrease in velocity due to the viscous effects in the boundary layer at $Z = 0.02m$.

The key observation from the plot is the approximate proportionality between corner radius and radial velocity. The radial velocity from the circular water tank is significantly higher than any of the square

tank designs. The results from the square tanks show that the smaller corner radius used for the geometry gives decreased radial velocity. The d/D ratio for all the cases from table 3.1 show there is correlation between corner radius and radial velocity. To determine the degree of proportionality, more cases should be considered in d/D ratios between $0.4 - 1.0$. It would then be reliable to determine a formulaic relation between d/D ratio and radial velocity.
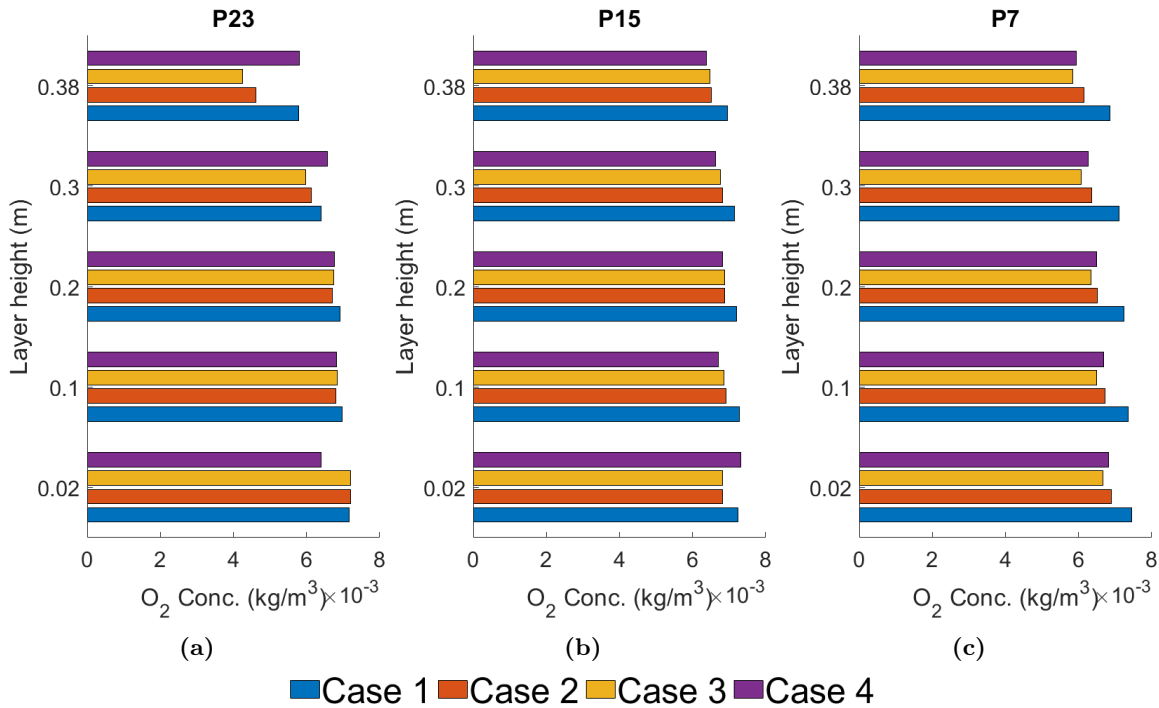

Figure 6.26: Comparison between radial velocity at probe locations across cases at $t = 3000s$

Figure 6.26 show the final concentrations recorded at the probes for all four geometries. It is evident there are similar levels of dissolved oxygen across all layers, however circular geometry has slightly higher concentrations among all cases. In figure 6.26a, the concentration for Case 4 is highest at the layers $Z = 0.30$ and $Z = 0.38$. This is due to the low concentration region formed at the wall which extends further outwards as seen in figure 6.13c compared to figure 6.19c

7   Conclusion and recommendation for future work

In the present study, numerical simulations have been performed to predict the dissolved oxygen transport in land-based aquaculture tanks with four different geometries. The numerical prediction of oxygen transport correlates well with experimental results as shown in the validation study, using data provided by Yin et al. (2021). The solver has been demonstrated to produce reliable results that can be used to predict oxygen transport for real world scenario with different aquaculture tanks.

In the study of water tank geometries, it is clear the circular geometry has shown to be most efficient for oxygen distribution. The square tanks have shown to be less efficient at transporting oxygen towards the center of the tanks due to reduced radial velocity of the fluid. The study has more potential in its analysis with the raw data gathered. The benefit of using visualizations of the simulations are a powerful tool to determine oxygen transport rather than relying on point-based measurements in real life. Being able to predict the flow direction and diffusion of oxygen based on tank geometry can therefore be determined without need for experimental measurements.

The primary work went into extracting results from the horizontal planes at different heights of the models, but vertical cross section planes are of interest when analyzing the oxygen concentration along walls or in cross section through the center of the tank. Parameters as functions of water depth are also worthwhile methods to process and present the data.

The present study has a broad range of topics that can be explored when decomposing the geometries investigated. Boundary layer flows in the corner fillets, inlet & outlet positions and solutions to saturating square tank geometries with oxygen.

For any future work based on the present study it seems that the simulations should be run to simulate 3600s to let the tanks reach an equilibrium state in oxygen concentration. This amendment may reveal a ceiling in oxygen concentration appearing at regions in the tanks, which were not decisively reached within $t = 3000s$. The larger volume of square geometries compared to the circular geometry means it takes longer to reach steady state fluid motion. This means the saturation can be viewed as time-dependent within the window of 3000 seconds of simulation.

References

Bergman, T. L., Lavine, A. S., Incropera, F. P., and Dewitt, D. P. (2011). *Fundamentals of Heat and Mass Transfer.* John Wiley & Sons, Inc.

George, W. K. (2013). Lectures in turbulence for the 21st century.

Misund, B. (2011). *Fiskeoppdrett.* Store Norske Leksikon. https://snl.no/fiskeoppdrett.

Moe, E., Skage, M., and Helsengreen, M. B. (2020). *The Norwegian Aquaculture Analysis 2020.* Ernst & Young.

Sander, R. (2015). *Compilation of Henry's law constants (version 4.0) for water as solvent*, volume 62.

Venvik, T. (2020). The state of world fisheries and aquaculture 2020.

Yin, G., Ong, M. C., and Jihoon Lee, T. K. (2021). Numerical study of oxygen transport in land-based aquaculture tank.